

# Solar Interior – Radial Structure, Rotation, Solar Activity Cycle

Axel Brandenburg

NORDITA, Roslagstullsbacken 23, AlbaNova University Center, 106 91  
Stockholm, Sweden [brandenb@nordita.dk](mailto:brandenb@nordita.dk)

**Summary.** Some basic properties of the solar convection zone are considered and the use of helioseismology as an observational tool to determine its depth and internal angular velocity is discussed. Aspects of solar magnetism are described and explained in the framework of dynamo theory. The main focus is on mean field theories for the Sun’s magnetic field and its differential rotation.

## 1 Introduction

The purpose of this chapter is to discuss the conditions that lead to the magnetic activity observed at the surface of the Sun. Only to a first approximation is the Sun steady and spherically symmetric. A more detailed inspection reveals fully three-dimensional small scale turbulent motions and magnetic fields together with larger scale flows and magnetic fields that lack any symmetry. The cause of the large scale and small scale magnetic fields, as well as large scale circulation and differential rotation, is believed to be the turbulent convection which, in turn, is caused by the increased radiative diffusivity turning much of the radiative energy flux into convective energy flux.

The magnetic field is driven by a self-excited dynamo mechanism, which converts part of the kinetic energy into magnetic energy. As in technical dynamos the term ‘self-excited’ refers to the fact that part of the electric power generated by induction is also used to sustain the ambient magnetic field around the moving conductors. How the conversion of kinetic energy into magnetic energy works will be discussed in some detail in this chapter. The kinetic energy responsible for this process can be divided into (i) small scale irregular turbulent motions (convection) and (ii) large scale differential rotation and meridional circulation. It is the anisotropy of the small scale motions that is responsible for making the rotation nonuniform. Furthermore, lack of mirror symmetry of the small scale motions is responsible for producing large scale magnetic fields. This process is explained in many text books, e.g. Moffatt (1978), Parker (1979), Krause & Rädler (1980), Stix (2002), or Rüdiger & Hollerbach (2004).

The magnetic field is also responsible for linking solar variability to natural climate variations on Earth. Changes in the Sun’s magnetic activity affect

the solar irradiance by only 0.1%, which is generally regarded as being too small to affect the climate. However, the UV radiation is more strongly modulated and may affect the climate. According to an alternative proposal, the Sun's magnetic field shields the galactic cosmic radiation, which may affect the production of nucleation sites for cloud formation that in turn affects the climate. Thus, an increase in the solar field strength increases the shielding, decreases the cosmic ray flux on Earth, decreases the cloud cover, and hence increases the temperature. This chain of events is rather simplified, and there can be drastically different effects from high or low clouds, for example. For a recent review of this rapidly developing field see Marsh & Svensmark (2000).

We begin by discussing the theoretical foundations governing the properties of turbulent convection zones, and discuss then helioseismology as an observational tool to determine, for example, the location of the bottom of the convection zone as well as the internal angular velocity. We turn then attention to the properties of the Sun's magnetic field and discuss dynamo theory as its theoretical basis. Magnetic field generation is caused both by the turbulent convection and by the large scale differential rotation, which itself is a consequence of turbulent convection, as will be discussed in the last section of this chapter. Only a bare minimum of references can be given here, and we have to restrict ourselves mostly to reviews which give an exhaustive overview of the original literature. Original papers are here quoted mainly in connection with figures used in the present text.

## 2 Radial structure

In order to determine the depth of the convection zone in the Sun and the approximate convective velocities it is necessary to solve the equations governing the radial structure of a star. For this purpose the Sun can be regarded as spherically symmetric. The equations governing the radial structure of the Sun (or a star) are quite plausible and easily derived. They can be written as a set of four ordinary differential equation, namely the

- equation for the Sun's gravitational field (Poisson equation),
- hydrostatic equilibrium (momentum equation),
- thermal equilibrium (energy equation),
- radiative equilibrium (radiation transport equation, convection).

These are given in all standard text books on stellar structure (e.g. Kippenhahn & Weigert 1990). In the following we discuss only a subset of these equations in order to describe some essential properties of the solar convection zone.

### 2.1 Global aspects

The rate of energy production of the Sun, i.e. its luminosity, is  $L_{\odot} = 4 \times 10^{26}$  W or  $4 \times 10^{33}$  erg s<sup>-1</sup>. The total intercepted by the Earth is only a small

fraction,

$$\frac{\pi R_E^2}{4\pi R_{E\odot}^2} = 4 \times 10^{-10}, \quad (1)$$

where  $R_E$  is the radius of the Earth (6400 km) and  $R_{E\odot}$  is the distance between the Earth and the Sun ( $= 1 \text{ AU} = 1.5 \times 10^{11} \text{ m}$ ). Thus, the total power reaching the projected surface of the Earth is  $4 \times 10^{-10} \times 4 \times 10^{26} \text{ W} = 1.6 \times 10^{17} \text{ W}$ . This is still a lot compared with the total global energy consumption, which was  $1.4 \times 10^{13} \text{ W}$  in the year 2001.

The total thermal energy content of the Sun can be approximated by half its potential energy (Virial theorem), i.e.

$$E_{\text{th}} \approx \frac{GM_{\odot}^2}{2R_{\odot}} = 2 \times 10^{41} \text{ J}, \quad (2)$$

where  $G \approx 7 \times 10^{-11} \text{ m}^3 \text{ kg}^{-1} \text{ s}^{-2}$  is Newton's constant,  $M_{\odot} \approx 2 \times 10^{30} \text{ kg}$  is the mass of the Sun, and  $R_{\odot} \approx 7 \times 10^8 \text{ m}$  is its radius. The time it would take to use up all this energy to sustain the observed luminosity is the Kelvin-Helmholtz time,

$$\tau_{\text{KH}} = E_{\text{th}}/L_{\odot} \approx 10^7 \text{ yr}, \quad (3)$$

which is long compared with time scales we could observe directly, but short compared with the age of the Sun and the solar system ( $5 \times 10^9 \text{ yr}$ ). Therefore, gravitational energy (which is extremely efficient in powering quasars!) cannot be the mechanism powering the Sun. This motivated the search for an alternative explanation, which led eventually to the discovery of the nuclear energy source of stars.

The similarity between gravitational and thermal energies can be used to estimate the central temperature of a star by equating  $GM/R = \mathcal{R}T_c/\mu$ . For the Sun this gives

$$T_c \sim \frac{\mu}{\mathcal{R}} \frac{GM}{R} = 1.5 \times 10^7 \text{ K} \quad (4)$$

for its central temperature. Here,  $\mathcal{R} \approx 8300 \text{ m}^2 \text{ s}^{-2} \text{ K}^{-1}$  is the universal gas constant and  $\mu \approx 0.6$  is the non-dimensional mean molecular weight for a typical mixture of hydrogen and helium. The estimate (4) happens to be surprisingly accurate. This relation also tells us that the central temperature of the Sun is only determined by its mass and radius, and not, as one might have expected, by the luminosity or the effectiveness of the nuclear reactions taking place in center of the Sun.

## 2.2 Thermal and hydrostatic equilibrium

The condition of hydrostatic equilibrium can be written in the form

$$0 = -\frac{1}{\rho} \nabla p + \mathbf{g}, \quad (5)$$

where  $\rho$  is the density,  $p$  is the pressure, and  $\mathbf{g}$  is the gravitational acceleration. In the spherically symmetric case we have  $\mathbf{g} = -(GM_r/r^2, 0, 0)$  in spherical polar coordinates, where  $M_r$  is the mass inside a sphere of radius  $r$ . Equation (5) is readily solved in the special case where the radial dependence of the density is polytropic, i.e.  $\rho(r) \sim T(r)^m$ , where  $m$  is the polytropic index. This yields

$$T(r) = T_c - \frac{1}{1+m} \frac{\mu}{\mathcal{R}} \int_0^r \frac{GM_r}{r^2} dr. \quad (6)$$

So, in the outer parts of the Sun, where  $M_r \approx \text{const}$ , equation (6) can be integrated, which shows that the temperature has a term that is proportional to  $1/r$ .

Significant amounts of energy can only be produced in the inner parts of the Sun where the temperatures are high enough for nuclear reactions to take place. The central temperature is characterized by the condition of thermal energy equilibrium, which quantifies the rate of change of the local luminosity,  $L_r$ , with radius. Outside the core, nuclear reactions no longer take place, so  $L_r$  can be considered constant. The radiative flux is given by  $F = L_r/(4\pi r^2)$ , which thus decreases like  $1/r^2$  in the outer parts.

In the bulk of the Sun, energy is transported by photon diffusion: the optical mean-free path is short compared with other relevant length scales (e.g. pressure scale height), so we are in the optically thick limit and can use the diffusion approximation for photons. The radiative flux,  $F$ , is therefore in the negative direction of and proportional to the gradient of the radiative energy density,  $aT^4$ , where  $a = 7.57 \times 10^{-15} \text{ erg cm}^{-3} \text{ K}^{-4}$  is the radiation-density constant. The connection between fluxes and concentration gradients is generally referred to as Fickian diffusion. As in kinetic gas theory, the diffusion coefficient is  $1/3$  times the typical particle velocity (=speed of light  $c$ ) and the mean free path  $\ell$  of the photons, so

$$F = -\frac{1}{3}c\ell \frac{d}{dr}(aT^4) = -\frac{4}{3}ac\ell T^3 \frac{dT}{dr} \approx -K \frac{dT}{dr}, \quad (7)$$

which is basically the condition of radiative equilibrium. Here we have introduced the radiative conductivity  $K$ . The photon mean free path is usually expressed in terms of the opacity  $\kappa$ , which is the effective cross-section per unit mass, so  $\ell = (\rho\kappa)^{-1}$ . Expressing  $a$  in terms of the Stefan-Boltzmann constant,  $\sigma_{\text{SB}} = ac/4$ , we have

$$K = \frac{16\sigma_{\text{SB}}T^3}{3\kappa\rho}. \quad (8)$$

An approximation for the opacity  $\kappa$  that is commonly used for analytic considerations is Kramer's formula

$$\kappa = \kappa_0 \rho T^{-7/2} \quad (\text{Kramer's opacity}), \quad (9)$$

where  $\kappa_0 = 6.6 \times 10^{18} \text{ m}^5 \text{ K}^{7/2} \text{ kg}^{-2}$  for so-called free-free transitions where two charged particles form a system which can absorb and emit radiation. This value may well be up to 30 times larger if the gas is rich in heavier elements, so it is a good electron supplier and bound-free processes (ionization of neutral hydrogen by a photon) become important as well. In practice, a good value is  $\kappa_0 \approx 10^{20} \text{ m}^5 \text{ K}^{7/2} \text{ kg}^{-2}$  (corresponding to  $10^{24} \text{ cm}^5 \text{ K}^{7/2} \text{ g}^{-2}$ ). With Kramer's formula, the conductivity is

$$K = \frac{16\sigma_{\text{SB}}T^{13/2}}{3\kappa_0\rho^2}. \quad (10)$$

For a polytropic stratification, i.e. when the density is given by a power law of the temperature,  $\rho \sim T^m$ , we have

$$K \sim T^{13/2-2m}, \quad (11)$$

which is constant for an effective polytropic index  $m = 13/4 = 3.25$ . This gives indeed a reasonable representation of the stratification of stars in convectively stable regions throughout the inner parts of the Sun. At the bottom of the solar convection zone the density is about  $200 \text{ kg m}^{-3}$  and the temperature is about  $2 \times 10^6 \text{ K}$ . This gives  $K = (3...100) \times 10^9 \text{ kg m s}^{-3} \text{ K}^{-1}$ . In order to carry the solar flux the average temperature gradient has to be around  $0.01 \text{ K/m}$ .

### 2.3 Transition to adiabatic stratification

In reality  $K$  does change slowly with height. Therefore the polytropic index effectively changes with height. If  $m < 13/4$ , then  $K$  decreases with decreasing  $T$ . However, in order to transport the required energy flux, the temperature gradient has to increase, so the polytropic index decreases further, until it reaches a critical value where the specific entropy gradient reverses sign. This leads to the onset of Rayleigh-Benard convection.

Specific entropy is an important quantity, because it does not change in the absence of local heating or cooling processes. For a perfect gas, and ignoring partial ionization effects, the specific entropy can be defined, up to a constant  $s_0$ , as

$$s = c_v \ln p - c_p \ln \rho + s_0, \quad (12)$$

where  $c_p$  and  $c_v$  are the specific heats at constant pressure and constant volume, respectively. Their ratio is  $\gamma = c_p/c_v$ , which is  $5/3$  for a monatomic gas, and their difference is  $c_p - c_v = \mathcal{R}/\mu$ .

If the specific entropy of the environment decreases in the upward direction, an upward moving blob of gas will develop excess entropy; see Figure 1. Assuming pressure equilibrium across the blob, equation (12) shows that a positive entropy excess  $\delta s$  corresponds to a density deficit,  $-c_p \delta \ln \rho$ . Thus, the blob will be lighter than its surroundings and will therefore be buoyant,

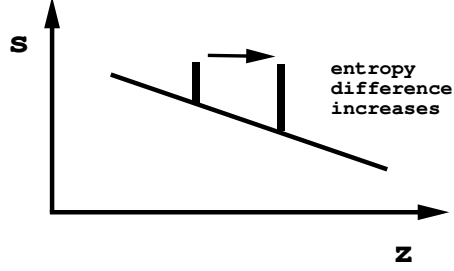


**Fig. 1.** Specific entropy profile for an unstable atmosphere. The difference in specific entropy between the blob and the surroundings increases as the blob ascends. Gravity points in the negative  $z$  direction, so  $\mathbf{g} \cdot \nabla s > 0$  in this case.

which drives the convection. Likewise, a downward moving blob will become heavier and fall even faster.

Using an equation of state for a perfect gas, i.e.  $p = (\mathcal{R}/\mu)\rho T$  we have  $d \ln p = d \ln \rho + d \ln T$ , and therefore equation (12) gives

$$\frac{\mu}{\mathcal{R}} \frac{ds}{d \ln T} = \frac{1}{\gamma - 1} - m. \quad (13)$$

This shows that, once  $m$  drops below  $1/(\gamma - 1) = 1.5$ , specific entropy decreases in the upward direction, i.e. in the direction of decreasing temperature. As a result, convection sets in which rapidly mixes the gas and causes the specific entropy to be nearly constant, keeping the effective value of  $m$  always close to the critical value of 1.5.

In order to calculate the actual stratification, we need to solve equations (5) and (7) together with the equations describing the increase of  $M_r$  and  $L_r$  with radius. Assuming that  $M_r$  and  $L_r$  are constant (valid far enough away from the core), we are left with two equations, which we express in terms of  $\ln p$  and  $\ln T$ , so

$$\frac{d \ln p}{dr} = -\frac{\mu}{\mathcal{R}T} \frac{GM_r}{r^2}, \quad (14)$$

$$\frac{d \ln T}{dr} = -\frac{1}{KT} \frac{L_r}{4\pi r^2}. \quad (15)$$

It is convenient to integrate these equations in the form

$$\frac{d \ln p}{dr} = -\frac{1}{H_p} \quad \text{and} \quad \frac{d \ln T}{dr} = -\frac{\nabla}{H_p}, \quad (16)$$

where the symbol  $\nabla$  is commonly used in astrophysics for the local value of  $d \ln T / d \ln p$ , and  $H_p = \mathcal{R}T/(\mu g)$  is the local pressure scale height. In the convectively stable regions, i.e. where  $m > 3/2$  (corresponding to  $\nabla < \nabla_{\text{ad}} =$

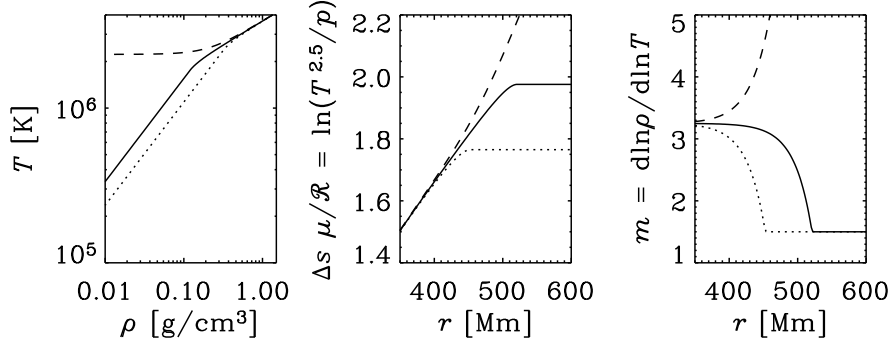


**Fig. 2.** Solutions of equations (16) and (17), starting the integration at  $r = 350$  Mm with  $T = 4 \times 10^6$  K and three different values of the density:  $\rho = 1.340$  (dashed line),  $\rho = 1.345$  (solid line), and  $\rho = 1.350$  (dotted line). The left hand panel shows temperature versus density. In this panel the integration goes from right to left (i.e. in the upward direction toward lower density). The middle panel shows the radial specific entropy profile; note that for the two cases with  $\rho \leq 1.345$  (solid and dotted lines) a convection zone develops at  $r \approx 500$  and  $420$  Mm, respectively. These two cases correspond to cases where  $m < 13/4$  at the lower boundary, as seen from the right hand panel. Note the positive entropy gradient indicating stability. In the last two panels the integration goes from left to right.

$2/5$ , and neglecting partial ionization effects), we have  $\nabla = \nabla_{\text{rad}}$ , where  $\nabla_{\text{rad}}$  can be found by dividing (15) by (14), so

$$\nabla_{\text{rad}} = \frac{1}{K} \frac{\mathcal{R}}{\mu} \frac{L_r}{4\pi G M_r}. \quad (17)$$

Inside convection zones, on the other hand,  $\nabla$  is replaced by  $\nabla_{\text{ad}}$ , so in general we can write  $\nabla = \min(\nabla_{\text{rad}}, \nabla_{\text{ad}})$ . In Figure 2 we show solutions obtained by integrating from  $r = 500$  Mm (1 Mm=1000km) upward using  $T = 4 \times 10^6$  K as starting value with  $\rho$  chosen such that the resulting value of  $m$  is either just below or just above  $13/4 = 3.25$ .

The considerations above have demonstrated that  $m$  must indeed be quite close to  $13/4 = 3.25$  in the radiative interior, but that its value decreases over a depth of about 50 Mm to the adiabatic value of 1.5 just below the bottom of the convection zone. The precise location of the bottom of the convection zone depends on the value of specific entropy in the bulk of the convection zone; see the middle panel of Figure 2. This value depends on the detailed surface physics and in particular the value of the opacity at the top of the convection zone. Here the Kramers opacity is no longer appropriate and the opacity from producing a negative hydrogen ion by polarizing a neutral hydrogen atom through a nearby charge becomes extremely important.

## 2.4 Mixing length theory and convection simulations

The approximation of setting  $\nabla = 2/5$  in the unstable region becomes poor near the surface layers where density is small and energy transport by turbulent elements less efficient. In fact, if the specific entropy were completely constant throughout the convection zone, there would be no net exchange of entropy by the turbulent elements. The definition for the convective flux is

$$\mathbf{F}_{\text{conv}} = \overline{(\rho \mathbf{u})' c_p T'}, \quad (18)$$

where overbars denote horizontal averages and primes denote fluctuations about these averages. A mean field calculation shows that  $\mathbf{F}_{\text{conv}}$  is proportional to the negative entropy gradient (see the monograph by Rüdiger 1989),

$$\mathbf{F}_{\text{conv}} = -\chi_t \bar{\rho} \bar{T} \nabla \bar{s} \quad (\text{if } \mathbf{g} \cdot \nabla \bar{s} > 0), \quad (19)$$

where  $\chi_t$  is a turbulent diffusion coefficient. In the following we omit the overbars for simplicity. Note that, by comparison with equation (7), in a turbulent environment Fickian diffusion down the *temperature* gradient gets effectively replaced by a similar diffusion down the *entropy* gradient. As with all other types of diffusion coefficients, the diffusion coefficient is proportional to the speed of the fluid parcels accomplishing the diffusion, and the length over which such parcels stay coherent (i.e. the mean free path which is commonly also denoted as the mixing length). Thus, we have

$$\chi_t = \frac{1}{3} u_{\text{rms}} \ell. \quad (20)$$

The subscript t indicates that this coefficient applies to turbulent transport of averaged fields. Given that the total flux is known, and also the fractional contribution from the radiative flux, we know also the convective flux. Thus, equation (19) can be used to determine the radial entropy gradient, provided we know  $\chi_t$ , and hence  $u_{\text{rms}}$  and  $\ell$ .

A natural length scale in the problem is the scale height, so we assume that the mixing length is some fraction  $\alpha_{\text{mix}}$  of the local vertical pressure scale height, i.e.

$$\ell = \alpha_{\text{mix}} H_p. \quad (21)$$

The scaling of the rms velocity is constrained by equation (18). Assuming that temperature and velocities are well correlated (warm always up, cool always down), we can also write

$$F_{\text{conv}} \approx \rho u_{\text{rms}} c_p \delta T, \quad (22)$$

where  $\delta T = (\overline{T'^2})^{1/2}$  is the rms temperature fluctuation. The relative proportion, with which convection produces velocity and temperature fluctuations, can be estimated by balancing the buoyancy force of a blob against its drag force, so  $F_{\text{buoy}} = F_{\text{D}}^{(\text{turb})}$  and therefore  $\delta \rho g V = C_D \rho u_{\text{rms}}^2 S$ , where  $C_D$  is the



drag coefficient,  $V$  is the volume of the blob, and  $S$  its cross-sectional area. We parameterize the ratio  $V/(C_D S) = \alpha_{\text{vol}} H_p$ , where  $\alpha_{\text{vol}}$  is a nondimensional factor of order unity characterizing the blob's volume to surface ratio. Assuming pressure equilibrium we have furthermore  $|\delta\rho/\rho| = |\delta T/T|$ , and

$$u_{\text{rms}}^2 = \alpha_{\text{vol}} g H_p \frac{\delta T}{T}. \quad (23)$$

Thus,  $u_{\text{rms}}$  is proportional to  $(\delta T/T)^{1/2}$ , so  $F_{\text{conv}}$  is proportional to  $(\delta T/T)^{3/2}$ , and therefore

$$\delta T/T \sim F_{\text{conv}}^{2/3} \quad \text{and} \quad u_{\text{rms}}/c_s \sim F_{\text{conv}}^{1/3}. \quad (24)$$

These scaling relations hold also locally at each depth; see Figure 3, where we show that in simulations of Rayleigh-Benard convection; the vertical profiles of the normalized mean squared vertical velocity,  $\langle u_z^2 \rangle/c_s^2$ , and of the relative temperature variance,  $\delta T/T$ , are indeed locally proportional to  $[F_{\text{conv}}/(\rho c_s^3)]^{2/3}$ . In Figure 3 the nondimensional coefficients are  $k_T \approx 1.1$  and  $k_u \approx 0.4$ , which implies

$$F_{\text{conv}} \approx k_u^{-3/2} \rho u_{\text{rms}}^3, \quad (25)$$

where  $k^{-3/2} \approx 4$  and  $\langle u_z^2 \rangle = u_{\text{rms}}^2$  has been used. Using  $F_{\text{conv}} = 7 \times 10^7 \text{ W m}^{-2}$  and  $\rho = 10 \text{ kg m}^{-3}$  at a depth of about 40 Mm this equation implies  $u_{\text{rms}} = 120 \text{ m s}^{-1}$ .

Using equation (19) and the fact that  $\chi_t \propto u_{\text{rms}} \propto F_{\text{conv}}^{1/3}$  we have  $F_{\text{conv}} \propto F_{\text{conv}}^{1/3} |ds/dz|$ , or<sup>1</sup>

$$|ds/dz| \propto F_{\text{conv}}^{2/3}. \quad (26)$$

In calculating the specific entropy gradient, we can, as a first approximation, assume that  $F_{\text{conv}}$  is approximately the total flux. However, it would not be difficult to calculate the entropy gradient self-consistently by solving a cubic equation. We also note that the entropy gradient is related to  $\nabla$  by

$$\frac{ds/c_p}{d \ln p} = \nabla - \nabla_{\text{ad}}, \quad \text{where} \quad \nabla_{\text{ad}} = 1 - \frac{1}{\gamma}. \quad (27)$$

A solution of the full system of equations, which include more realistic physics than what has been described here, has been given by Spruit (1974); see Table 1. The rms velocities are about half as big as expected from equation (25).

Near and beyond the upper and lower boundaries of the convection zones the approximation (23) becomes bad, because it ignores the fact that convective elements have inertia and can therefore overshoot a significant distance

<sup>1</sup> A more rigorous calculation using the equations above shows that

$$\frac{ds/c_p}{dz} = -\frac{k}{H_p} \left( \frac{F_{\text{tot}}}{\rho c_s^3} \right)^{2/3}, \quad \text{where} \quad k = 3 \frac{\gamma - 1}{\alpha_{\text{mix}}} \left[ \alpha_{\text{vol}} \left( 1 - \frac{1}{\gamma} \right) \right]^{-1/3},$$

and  $k \approx 1$  for  $\alpha_{\text{mix}} = \alpha_{\text{vol}} = 2$ .

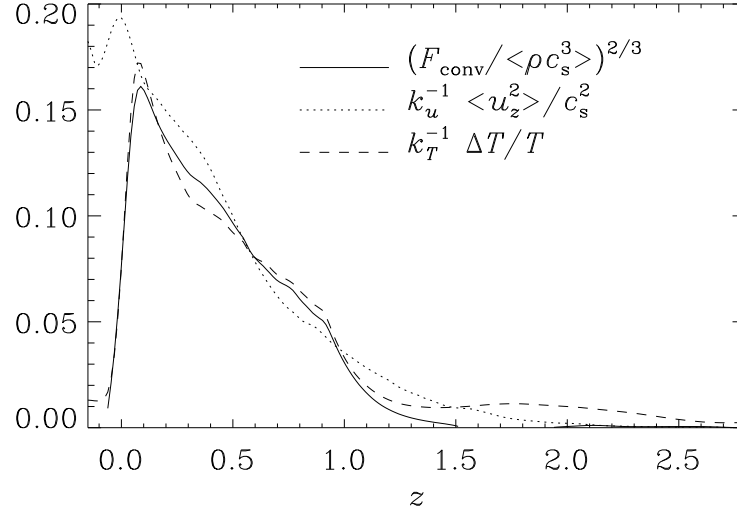


**Fig. 3.** Vertical profiles of the normalized mean squared vertical velocity fluctuations and temperature fluctuations, compared with the normalized convective flux raised to the power 2/3. Note the good agreement between the three curves within the convection zone proper. In this plot,  $z$  denotes depth. The positions  $z = 0$  and 1 corresponds to the top and bottom of the convection zone, respectively. There is a lower overshoot layer for  $z > 1$  and an upper overshoot layer for  $z < 0$ . [Adapted from Brandenburg et al. (2005).]

into the stably stratified regions. In those layers where the entropy gradient has reversed, a downward moving fluid parcel becomes hotter than its surroundings. Thus, in these layers the convection carries convective flux downward, so its sign is reversed. Simulations have clearly demonstrated that, owing to strong stratification, convection will be highly inhomogeneous, with narrow downdrafts and broad upwellings. This leads to a characteristic (but irregular) pattern of convection; see, e.g., the text book by Stix (2002).

**Table 1.** The solar mixing length model of Spruit (1974).

$z$ [Mm]	$T$ [K]	$\rho$ [g cm <sup>-3</sup> ]	$H_p$ [Mm]	$u_{\text{rms}}$ [m/s]	$\tau$ [d]	$\nu_t$ [cm <sup>2</sup> /s]	$\Omega_0 \tau$
24	$1.8 \times 10^5$	0.004	8	70	1.3	$1.5 \times 10^{12}$	0.6
39	$3.0 \times 10^5$	0.010	13	56	2.8	$2.0 \times 10^{12}$	1.3
155	$1.6 \times 10^6$	0.12	48	25	22	$3.2 \times 10^{12}$	10
198	$2.2 \times 10^6$	0.20	56	4	157	$0.6 \times 10^{12}$	70

The precise location of the bottom of the convection zone is now fairly well determined from detailed models of stellar structure, where the full evolution from a zero-age main sequence star to a chemically evolved star where some of the hydrogen has been burnt into helium and other elements, has been taken into account. An even more accurate and quite independent determination of the bottom of the convection zone and the overall stratification is possible through helioseismology. This will be discussed in the next section.

### 3 Helioseismology

The Sun exhibits so-called five-minute oscillations that are best seen in spectral line shifts. These oscillations were first thought to be the oscillatory response of the atmosphere to convection granules pushing upwards into stably stratified layers. This idea turned out to be wrong, because the oscillations are actually *global* oscillations penetrating deep layers of the Sun. In fact, they are just sound waves that are *trapped* in a cavity formed by reflection at the top and refraction in deeper layers. At the top, sound waves cannot penetrate if their wave length exceeds the scale on which density changes. The refraction in deeper layers is caused by the higher wave speed of the wave front in those parts that are deeper in the Sun. This makes the wave front bend back up again.

The decisive observation came when a wavenumber–frequency (or  $k$ – $\omega$ ) diagram was produced that showed that these modes have long term and large scale spatio-temporal coherence with wavenumbers corresponding to 20–60 Mm; see Figure 4.

By now the determination of  $k$ – $\omega$  diagrams has grown to a mature and standard tool in solar physics.

#### 3.1 Qualitative description

Since the beginning of the eighties, standing acoustic waves in the Sun have been studied in great detail. It has become possible to measure directly (i.e. without the use of a solar model)

- (i) the radial dependence of the sound speed,  $c_s(r)$ , which is proportional to the temperature. Note that  $c_s^2 = \gamma p / \rho = \gamma \mathcal{R} T / \mu$ , but the mean molecular weight increases near the core due to the nuclear reaction products.
- (ii) the radial and latitudinal dependence of the internal angular velocity,  $\Omega = \Omega(r, \theta)$ , throughout the Sun.

This technique is called *helioseismology*, because it is mathematically similar to the techniques used in seismology of the Earth's interior. Qualitatively, the radial dependence of the sound speed can be measured, because standing sound waves of different horizontal wave number penetrate to different

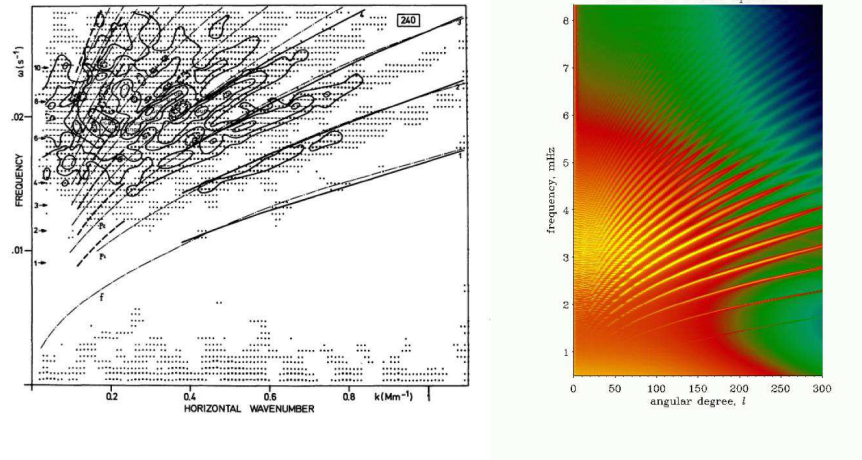


**Fig. 4.** Comparison between the  $k_h$ - $\omega$  (or  $l$ - $\nu$ ) diagrams obtained by Deubner in 1975 (left), and by the SOHO/MDI team in 2000 (right). The figure by Deubner, where he compares observations with the predictions by Ulrich (1970, solid lines), proved that the 5-min oscillations were global modes. Courtesy F.-L. Deubner (left) and P. Scherrer (right).

depths. Therefore, the frequencies of those different waves depend on how exactly the sound speed changes with depth. Since the Sun rotates, the waves that travel in the direction of rotation (i.e. toward us) are blue-shifted, and those that travel against the direction of rotation (i.e. away from us) are red-shifted. Therefore, the frequencies are split, depending on the amount of rotation in different layers. There are many reviews on the subject (e.g., Demarque & Guenther 1999). Here we follow the text book by Stix (2002).

Acoustic waves are possible, because they are constantly being excited by the “noise” generated in the convection zone via stochastic excitation. The random fluctuations in the convection are turbulent and contain power at all frequencies. Now the Sun is a harmonic oscillator for sound waves and the different sound modes can be excited stochastically.

Helioseismology has now grown to be immensely sophisticated and more accurate data have emerged from observations with the Michelson Doppler Imager aboard the SOHO spacecraft, located at the inner Lagrange point between Sun and Earth, and also the GONG project (GONG = Global Oscillation Network Group). The latter involves six stations around the globe to eliminate nightly gaps in the data.

### 3.2 Inverting the frequency spectrum

As with a violin string, the acoustic frequency of the wave increases as the wavelength decreases. More precisely, the frequency is given by  $\nu = c_s/\lambda$ , where  $\lambda$  is the wavelength and  $c_s$  is the sound speed. We will also use the circular frequency  $\omega = 2\pi\nu$  with  $\omega = c_s k$ , where  $k = 2\pi/\lambda$  is the wavenumber. If sound waves travel an oblique path then we can express the wavenumber in terms of its horizontal and vertical wavenumbers,  $k_h$  and  $k_v$ , respectively. We do this because only the horizontal wavenumber can be observed. This corresponds to the horizontal pattern in Figure 4. Thus, we have

$$k^2 = k_h^2 + k_v^2. \quad (28)$$

The number of radial nodes of the wave is given by the number of waves that fit into that part of the Sun where the corresponding wave can travel. This part of the Sun is referred to as the cavity. The larger the cavity, the more nodes there are for a given wavelength. The number of modes  $n$  is given by

$$n = 2\Delta r/\lambda = 2\Delta r \frac{k_v}{2\pi} = \Delta r k_v/\pi, \quad (29)$$

where  $\Delta r$  is the depth of the cavity. If the sound speed and hence  $k_v$  depend on radius, this formula must be generalized to

$$n = \frac{1}{\pi} \int_{r_{\min}}^{R_{\odot}} k_v dr, \quad (30)$$

supposing the cavity to be the spherical shell  $r_{\min} < r < R_{\odot}$ .

The horizontal pattern of the proper oscillation is described by spherical harmonics with indices  $l$  and  $m$ , hence the horizontal wavenumber is

$$k_h^2 = \frac{\ell(\ell+1)}{r^2}, \quad (31)$$

and we can write

$$k_v = \sqrt{\frac{\omega_{nl}^2}{c_s^2} - \frac{\ell(\ell+1)}{r^2}} = \frac{\omega_{nl}}{r} \sqrt{\frac{r^2}{c_s^2} - \frac{\ell(\ell+1)}{\omega_{nl}^2}}. \quad (32)$$

where the subscripts of  $\omega_{nl}$  denote the radial order  $n$  and the spherical harmonic degree  $l$  of the modes. Therefore, the number  $n$  of radial nodes is given by

$$\frac{\pi(n+\alpha)}{\omega_{nl}} = \int_{r_{\min}}^{R_{\odot}} \sqrt{\frac{r^2}{c_s^2} - \frac{\ell(\ell+1)}{\omega_{nl}^2}} \frac{dr}{r}, \quad (33)$$

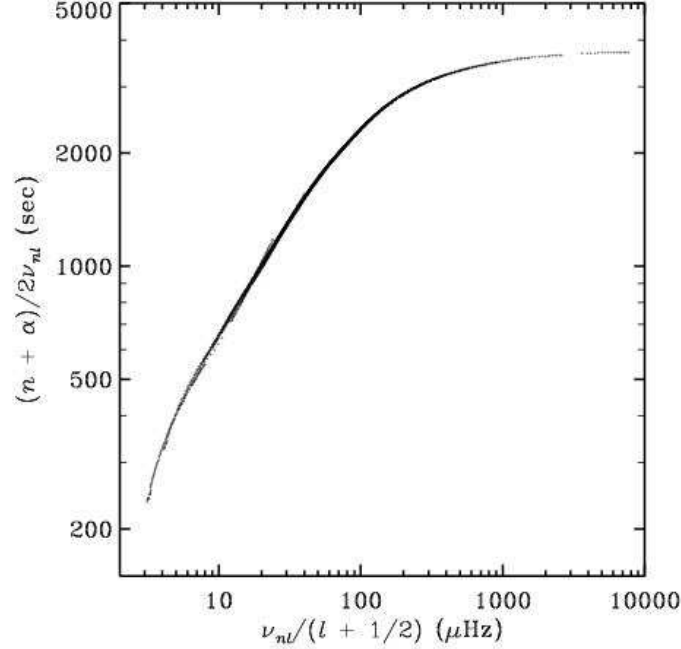


**Fig. 5.** The Duvall law. The vertical axis (ordinate) corresponds to  $F$  in equation (37) and the horizontal axis (abscissa) is basically  $u^{-1}$ . He found this law well before its significance was understood in terms of one of the functions in Abel’s integral transformation. [Courtesy J. Christensen-Dalsgaard et al. (1985).]

where an empirically (or otherwise) determined phase shift  $\alpha \approx 1.5$  accounts for the fact that the standing waves are confined by barriers that are “soft” and extended, rather than rigid and fixed.

The location of the inner turning radius is given by the point where the wavevector has become completely horizontal. Using

$$\omega_{nl}^2/c_s^2 = k^2 = k_h^2 + k_v^2, \quad (34)$$

together with  $k_v = 0$  at  $r = r_{\min}$  and  $k_h^2 = \ell(\ell+1)/r^2$ , we have  $(r_{\min}/c_s)^2 = \ell(\ell+1)/\omega_{nl}^2$ . This implies that

$$r_{\min} = \frac{c_s}{\omega_{nl}} \sqrt{\ell(\ell+1)}, \quad (35)$$

so only modes with low  $\ell$  values have turning points close to the center and can be used to examine the Sun’s core. We now introduce new variables

$$\xi = \frac{r^2}{c_s^2}, \quad u = \frac{\ell(\ell+1)}{\omega_{nl}^2}, \quad (36)$$

so the inner turning point of the modes corresponds to  $\xi = u$ . Furthermore, we denote the left hand side of equation (33) by  $F(u)$ , so we can write

$$F(u) = \int_u^{\xi_\odot} \sqrt{\xi - u} \frac{d \ln r}{d \xi} d \xi, \quad (37)$$

where the location of the inner refraction point corresponds to  $u = \xi$ . The function  $F(u)$  was obtained from observations by Duvall (1982) on the grounds that this combination of data makes the different branches collapse onto one (see Figure 5). He discovered this well before its significance was understood by Gough (1985) several years later.

Since we know  $F(u)$  from observations and are interested in the connection between  $r$  and  $\xi$  (i. e.  $r$  and  $c_s$ ), we interpret (37) as an integral equation for the unknown function  $r(\xi)$ . Most integral equations cannot be solved in closed form, but this one can. Gough (1985) realized that it can be cast in the form of Abel's integral equation. The pair of complementary equations (primes denote derivatives) is

$$F(u) = \int_u^{\xi_\odot} \sqrt{\xi - u} G'(\xi) d \xi, \quad (38)$$

$$G(\xi) = \frac{2}{\pi} \int_\xi^{\xi_\odot} \frac{1}{\sqrt{\xi - u}} F'(u) du. \quad (39)$$

Inserting the definitions for  $\xi$  and  $u$  into equation (39), we obtain

$$\int_\xi^{\xi_\odot} \frac{F'(u)}{\sqrt{u - \xi}} du = -\frac{\pi}{2} \int_\xi^{\xi_\odot} \frac{d \ln r}{d \xi'} d \xi' = -\frac{\pi}{2} \ln r \Big|_{\xi'=\xi}^{\xi_\odot} = \frac{\pi}{2} \ln \frac{r(\xi)}{R_\odot}. \quad (40)$$

This equation can be solved for  $r = r(\xi)$ :

$$r(\xi) = R_\odot \exp \left( \frac{2}{\pi} \int_\xi^{\xi_\odot} \frac{F'(u)}{\sqrt{u - \xi}} du \right). \quad (41)$$

This is the final result of inverting the integral equation (37). It establishes the link between the observable function  $F(u)$  and the function  $r(\xi)$ , from which the radial profile of the sound velocity  $c_s$  can be obtained. Figure 6 gives the result of an inversion procedure that computes the radial dependence of the sound speed on depth, using the detailed frequency spectrum as input.

It should be noted, however, that this approach is usually not practical when input data are noisy. Instead, a minimization procedure is often used

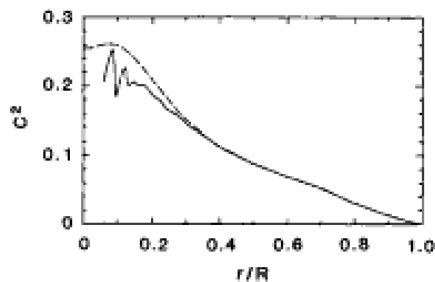


**Fig. 6.** Radial dependence of the sound speed on radius in the Sun. Note the change in slope near a radius of 0.7 solar radii. The oscillations near the center are not physical. The theoretical model (dotted line) is in fair agreement with the direct measurements. The sound speed has its maximum not in the center, because the mean molecular weight  $\mu$  increases towards the center, which causes  $c_s$  to decrease. (We recall that  $c_s^2(r) = \gamma \mathcal{R}T/\mu$ .) [Adapted from Stix (2002).]

where the resulting function is by construction smooth. This procedure falls under the general name of *inverse theory* and is frequently used in various branches of astrophysics.

Historically, the model independent determination of the sound speed and thereby the temperature in the center of the Sun has been important in connection with understanding the origin of the solar neutrino problem. In fact, the solar neutrino flux was measured to be only one third of that originally expected. A lower core temperature could have resolved this mismatch, but this possibility was then ruled out by helioseismology. Now we know that there are neutrino oscillations leading to a continuous interchange between the three different neutrino species, which explains the observed neutrino flux of just one species.

### 3.3 The solar abundance problem

Opacities depend largely on the abundance of heavier elements. The solar models calculated with the old tables agreed quite well using the conventional abundance ratio of heavier elements to hydrogen,  $Z/X = 0.023$ . However, the abundancies were based on fits of observed spectra to synthetic line spectra calculated from model atmospheres. These models parameterize the three-dimensional convection only rather crudely. New synthetic line spectra calculated from three-dimensional time-dependent hydrodynamical models of the solar atmosphere give a lower value of the solar oxygen abundance. With the new values ( $Z/X = 0.017$ ) it became difficult to reconcile the previously good agreement between stellar models and helioseismology. The solution to this problem is still unclear, but there is now evidence that the solar neon



abundance may have been underestimated. A neon abundance enhanced by about 2.5 is sufficient to restore the good agreement found previously.

The detailed stratification depends quite sensitively on the equation of state,  $p = p(\rho, T)$ . However, the uncertainties in the theoretically determined equation of state are now quite small and cannot be held responsible for reconciling the helioseismic mismatch after adopting the revised solar abundancies.

### 3.4 Internal solar rotation rate

Another important problem is to calculate the internal rotation rate of the Sun (Figure 7). This has already been possible for the past 20 years, but the accuracy has been ever improving. We will not discuss here the mathematics in any further detail, but refer instead to the review by Thompson et al. (2003). The basic technique involves the prior calculation of kernel functions,  $K_{nlm}(r, \theta)$ , that are independent of  $\Omega$ , such that the rotational frequency splitting can be expressed as

$$\omega_{nlm} - \omega_{nl0} = m \int_0^R \int_0^\pi K_{nlm}(r, \theta) \Omega(r, \theta) r dr d\theta \quad (42)$$

Several robust features that have emerged from the work of several groups include

- The contours of constant angular velocity do not show a tendency of alignment with the axis of rotation, as one would have expected, and as many theoretical models still show.
- The angular velocity in the radiative interior is nearly constant, so there is no rapidly rotating core, as has sometimes been speculated.
- There is a narrow transition layer at the bottom of the convection zone, where the latitudinal differential rotation goes over into rigid rotation (i.e. the tachocline). Below  $30^\circ$  latitude the radial angular velocity gradient is here positive, i.e.  $\partial\Omega/\partial r > 0$ , in contrast that what is demanded by conventional dynamo theories.
- Near the top layers (outer 5%) the angular velocity gradient is negative and quite sharp.

A completely model-independent knowledge about the internal rotation rate of the Sun has proved to be invaluable for the theory of the magnetic field in the Sun, for its rotation history, and for solar dynamo theory. Prior to the advent of helioseismology some 25 years ago, the idea of a rapidly rotating core was quite plausible, because at birth the Sun is believed to have spun at least 50 times faster than now, and because in the Sun the viscous time scale exceeds the age of the Sun. The fact that also the core has spun down means that there must be some efficient torques accomplishing the angular momentum transport inside the Sun. A likely candidate is the magnetic field.

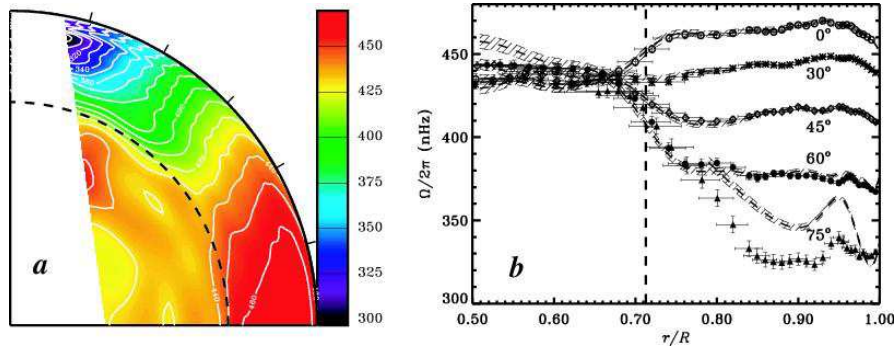


**Fig. 7.** Angular velocity profile in the solar interior inferred from helioseismology (after Thompson et al. 2003). In panel (a) a two-dimensional (latitude-radius) rotational inversion is shown based on the Subtractive Optimally Localized Averaging (SOLA) technique. In panel (b) the angular velocity is plotted as a function of radius for several selected latitudes, based on both SOLA (symbols, with  $1\sigma$  error bars) and regularized least squares (RLS; dashed lines) inversion techniques. Dashed lines indicate the base of the convection zone. All inversions are based on data from the Michelson Doppler Imager aboard the SOHO spacecraft, averaged over 144 days. Inversions become unreliable close to the rotation axis, represented by white areas in panel (a). Note also that global modes are only sensitive to the rotation component which is symmetric about the equator (courtesy M.J. Thompson et al. 2003).

It is indeed well known that only a weak poloidal field is needed to brake the rotation of the radiative interior.

Helioseismology has indicated that the transition from latitudinal differential rotation in the bulk of the convection zone to nearly rigid rotation in the radiative interior is relatively sharp. This transition region is called the tachocline. The idea of a sharp transition region has problems of its own, because viscous spreading would tend to smooth the transition with time. The solution to this problem was thought to be related to the effect of a mostly horizontal turbulence. However, it can be argued that the rigidity of the radiative interior is constantly maintained by the presence of a weak magnetic field of about 1 G; see Rüdiger & Hollerbach (2004) for a recent monograph covering also this aspect.

### 3.5 Local helioseismology

At larger values of  $\ell$  the coherence time of the waves becomes rather short and the modes are no longer global and take on a more local character. There are various techniques that use these modes to extract information about local variations of sound speed and local flows. The most popular method is the ring diagram technique. For a detailed review see Gizon & Birch (2005). Among other things this method has demonstrated the presence of converging

flows around sunspots and a rather shallow temperature subsurface structure. However, a serious shortcoming of the present approach is the neglect of magnetosonic and Alfvén waves.

## 4 Solar activity cycle

In the following we discuss some basic properties of the solar magnetic field. Its main feature is the 11 year cycle, as manifested in the (approximately) eleven year variation of the sunspot number. Sunspots are associated with sites of a strong magnetic field of about 2–3 kG peak field strength. Sunspots appear typically at about  $\pm 30^\circ$  latitude at the beginning of each cycle, i.e. when the sunspot number begins to rise again. During the course of the cycle, spots appear at progressively lower latitudes. At the end of the cycle, sunspots appear at low latitudes of about  $\pm 4^\circ$ . Again, detailed references cannot be given here, but we refer to the paper by Solanki et al. (2006) for a recent review.

### 4.1 The butterfly diagram

Although the detailed mechanism of their formation is still uncertain, it seems that sunspots form when a certain threshold field is exceeded, so they occur usually only below  $\pm 30^\circ$  latitude. However, magnetic fields can still be detected at higher latitudes all the way up to the poles using the Zeeman effect. Figure 8 shows, as a function of latitude and time, the normal component of the azimuthally averaged surface field,  $\overline{B}(R_\odot, \theta, t)$ , where

$$\overline{B}(r, \theta, t) = \int_0^{2\pi} B \frac{d\phi}{2\pi}. \quad (43)$$

Such diagrams, which can also be produced for the mean number of sunspots as function of time and latitude, are generally referred to as butterfly diagrams.

Although the field strength in sunspots is about 2 kG, when the field is averaged in longitude only a small net field of about  $\pm 20$  G remains. Near the poles the magnetic field is more clearly defined because it fluctuates less strongly in time near the poles than at lower latitudes. A characteristic feature is that the polar field changes sign shortly after each sunspot maximum.

At intermediate latitudes  $|\cos \theta| = 0.5 \dots 0.7$ , corresponding to a latitude,  $90^\circ - \theta$ , of  $\pm(30^\circ \dots 45^\circ)$ , there are characteristic streaks of magnetic activity that seem to move poleward over a short time ( $\sim 1 \dots 2$  yr). These streaks are rather suggestive of systematic advection by poleward meridional circulation near the surface. This indicates that the streaks are really just a consequence of the remaining flux of decaying active regions being advected poleward from lower latitudes. Looking at a plot of the magnetic field at poorer resolution

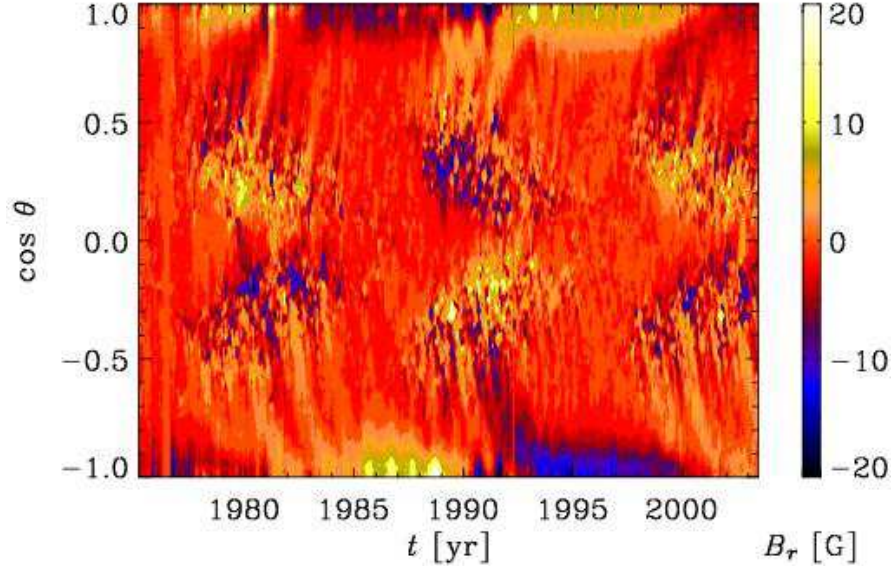


**Fig. 8.** Longitudinally averaged radial component of the observed solar magnetic field as a function of  $\cos(\text{colatitude})$  and time. Dark shades denote negative values and light shades denote positive values. Note the sign changes both in time and across the equator (courtesy of R. Knaack).

would show what is known as the polar branch, whose presence has been found previously through various other proxies (e.g. through the migration of the line where prominences occur). This has been reviewed in detail by Stix (1974).

In summary, the cyclic variation of the field together with its latitudinal migration, and the alternating orientation of bipolar magnetic regions are the main systematic properties of the solar magnetic field. In § 5 we discuss theoretical approaches to the present understanding of this phenomenon.

## 4.2 Cyclic activity on other solar-like stars

It should be noted that magnetic activity and activity cycles are not unique to the Sun. In fact, many stars with outer convection zones display magnetic activity, as is evidenced by proxies such as the H and K line emission within the Calcium absorption line. This H and K line emission is caused by hot plasma that is confined in the magnetic flux tubes in the coronae of these stars. Among the solar-like stars of spectral type G and solar-like rotation, many have cyclic magnetic activity while others show time-independent magnetic activity that is believed to be associated with the possibility that these stars are in a grand minimum, such as the famous Maunder minimum.

### 4.3 Grand minima

Grand minima are recurrent states of global magnetic inactivity of a star. This behavior may be associated with the chaotic nature of the underlying dynamo process. For the Sun this behavior is evidenced through the record of the Carbon 14 isotope concentrations in tree rings as well as through the Beryllium 10 isotope concentrations of ice core drillings from Greenland. It is interesting to note that during the Maunder minimum between 1645 and 1700 the magnetic activity was not completely suppressed;  $^{10}\text{Be}$  still show cyclic variability, albeit with a somewhat longer period of about 15 years. Shortly after the Sun emerged from the Maunder minimum the sunspot activity was confined only to the northern hemisphere. This type of latitudinal asymmetry has been seen in some dynamo models that display sporadically a mixture of modes that are symmetric and antisymmetric about the equator. For the Sun, some of the earlier grand minima have specific names such as the Spörer minimum (1420–1530), the Wolf Minimum (1280–1340), and the Oort minimum (1010–1050).

Grand minima can be important for the Earth's climate. For example the Maunder minimum is associated with the 'Little Ice Age' that occurred from 1560 to 1850. During the 500 years before that the Sun was particularly active as is evidenced by the high levels of  $^{14}\text{C}$  production: this was the period when wine was made from grapes grown in England and when the Vikings colonized Greenland.

By combining different proxies of solar activity, several typical time scales can be identified, the Schwabe 11-year cycle, the 88-year Gleissberg cycle, the 205-year De Vries cycle, and the 2100 or 2300 year Hallstatt cycle.

### 4.4 Active regions and active longitudes

Active regions are complexes of magnetic activity out of which sunspots, flares, coronal mass ejections, and several other phenomena emerge with some preference over other regions. These regions tend to be bipolar, i.e. they come in pairs of opposite polarity and are roughly aligned with the east–west direction.

Over periods of up to half a year active regions appear preferentially at the same longitude and follow a latitude-dependent rotation law. An analysis of solar magnetograms show that at the beginning of each cycle, when most of the activity occurs at about  $\pm 30^\circ$  latitude, the rotation rate of the active longitudes is less than at the end of each cycle, when the typical latitude is only  $\pm 4^\circ$  latitude. There are various reports that these longitudes might be stable over longer periods of time (so-called active longitudes), but this is still very much a matter of debate.

The notion of field line anchoring is occasionally used in connection with sunspot proper motions. Long before the internal angular velocity was determined via helioseismology, it was known that sunspots rotate faster than the

surface plasma. Moreover, young sunspots rotate faster than old sunspots. A common interpretation is that young sunspots are still anchored at a greater depth than older ones, and that therefore the internal angular velocity must decrease with height. This provided also the basis for the classical mean field dynamo theory of the solar cycle according to which the radial angular velocity gradient has to be negative. This will be discussed in more detail in § 5.

With the advance of helioseismology, it has become clear that at low latitudes the angular velocity decreases with radius throughout the bulk of the convection zone. A negative radial gradient exists only in the upper 30 Mm (sometimes referred to as the supergranulation layer). Indeed, the very youngest sunspots have a rotation rate that is comparable to or even slightly in excess of the fastest angular velocity seen with helioseismology anywhere in the Sun (i.e. at  $r/R_\odot \approx 0.95$ ).

#### 4.5 Torsional oscillations

At the solar surface the angular velocity varies with the 11 year cycle. In other words,  $\overline{\Omega}$  at the surface (at  $r = R_\odot$ ) is not only a function of colatitude  $\theta$ , but also of time. The pattern of  $\overline{\Omega}(R_\odot, \theta, t)$  shows an equatorward migration, similar to the butterfly diagram of the mean poloidal magnetic field in Figure 8. Helioseismology has now established that this pattern extends at least half way into the convection zone. At the bottom of the convection zone the 11 year variation is not (yet?) observed, but there is possibly a 1.3 year modulation of the local angular velocity, although this is still unclear and debated (see the review by Thompson et al. 2003). In recent years this 1.3 year modulation has gone away, but it has been speculated that the presence of a modulation may depend on the phase in the cycle.

The 11 year cyclic modulation is known as torsional oscillation, but model calculations demonstrate that these oscillations can be understood as a direct response to the varying magnetic field. The amplitude of the torsional oscillations is about 8%, suggesting that magnetic effects must be moderate and the fields of sub-equipartition strength.

### 5 Dynamo theory

Given that the magnetic decay times in astrophysical plasmas are generally very long, there have been a number of attempts in the literature to explain the Sun's magnetic field in terms of a primordial, frozen-in field. Such approaches tend to be rather sketchy when it comes to predicting any quantitative details that can be tested. Dynamo theory, on the other hand, provides a self-consistent framework of magnetic field generation in general that can be tested against direct simulations. Owing to the turbulent nature of the

flows, such dynamos are generally referred to as “turbulent dynamos”. Unfortunately, early simulations did not reproduce the solar behavior very well. The reason for this may simply be that, for example, the resolution was insufficient to capture important details. The failure to explain the observations has led to a number of ad hoc assumptions and modifications that are not satisfactory. At the same time, dynamo theory itself has experienced some important extensions that followed from trying to explain a long standing mismatch between simulations and theory, even under rather idealized conditions such as forced turbulence in a periodic domain. In this section we can only outline the basic aspects of dynamo theory. For a more extensive review, especially of the recent developments, see Ossendrijver (2003) and Brandenburg & Subramanian (2005).

### 5.1 The induction equation

At the heart of dynamo theory is the induction equation, which is just the Faraday equation together with Ohm’s law, i.e.

$$\frac{\partial \mathbf{B}}{\partial t} = -\nabla \times \mathbf{E} \quad \text{and} \quad \mathbf{J} = \sigma (\mathbf{E} + \mathbf{U} \times \mathbf{B}), \quad (44)$$

respectively. The initial conditions furthermore must obey  $\nabla \cdot \mathbf{B} = 0$ . Eliminating  $\mathbf{E}$  yields

$$\frac{\partial \mathbf{B}}{\partial t} = \nabla \times (\mathbf{U} \times \mathbf{B} - \mathbf{J}/\sigma). \quad (45)$$

Then, using Ampere’s law (ignoring the Faraday displacement current),  $\mathbf{J} = \nabla \times \mathbf{B}/\mu_0$ , where  $\mu_0$  is the vacuum permeability, one obtains the induction equation in a form that reveals the diffusive nature of the last term as  $\dots + \eta \nabla^2 \mathbf{B}$ , where  $\eta = (\sigma \mu_0)^{-1}$ .

A complete theory of magnetic field evolution must include also the momentum equation, because the magnetic field will react back on the velocity field through the Lorentz force,  $\mathbf{J} \times \mathbf{B}$ , so

$$\rho \frac{D\mathbf{U}}{Dt} = -\nabla p + \mathbf{J} \times \mathbf{B} + \mathbf{F}, \quad (46)$$

together with the continuity equation,  $\partial \rho / \partial t = -\nabla \cdot (\rho \mathbf{U})$ . In equation (46),  $\mathbf{F}$  subsumes a range of possible additional forces such as viscous and gravitational forces, as well as possibly Coriolis and centrifugal forces.

To study the dynamo problem, the complete set of equations is often solved using fully three-dimensional simulations both in Cartesian and in spherical geometries. Especially in early papers, the continuity equation has been replaced by the incompressibility condition,  $\nabla \cdot \mathbf{U} = 0$ , or by the anelastic approximation,  $\nabla \cdot (\rho \mathbf{U}) = 0$ . In both cases,  $\rho$  no longer obeys an explicitly time-dependent equation, and yet  $\rho$  can of course change via the equation of state (pressure and temperature are still changing). These approximations are technically similar to that of neglecting the Faraday displacement current.

As long as the magnetic field is weak, i.e.  $B^2/\mu_0 \ll \rho U^2$  at all scales and all locations, it may be permissible to assume  $\mathbf{U}$  as given and to solve only the induction equation for  $\mathbf{B}$ . This is called the kinematic dynamo problem.

Meanwhile some types of dynamos have been verified in experiments. One is the Ponomarenko-like dynamo that consists of a swirling flow surrounded by a nonrotating counterflow (Gailitis et al. 2001). The flow is driven by propellers and leads to self-excited dynamo action when the propellers exceed about 1800 revolutions per minute (30 Hz), producing peak fields of up to 1 kG. Another experiment consists of an array of 52 connected tubes with an internal winding structure through which liquid sodium is pumped, making the flow strongly helical with nearly uniform kinetic helicity density within the dynamo module containing the pipes (Stieglitz & Müller 2001). Such a flow is particularly interesting because it allows meaningful averages to be taken, making this problem amenable to a mean field treatment. The mean field approach is important in solar physics and will be discussed in § 5.3. First, however, we discuss the case where no mean field is produced and only a small scale field may be generated.

## 5.2 Small scale dynamo action

There is an important distinction between small scale and large scale turbulent dynamos. This is mainly a distinction by the typical scale of the field. Both types of dynamos have in general a turbulent component, but large scale dynamos have an additional component on a scale larger than the typical scale of the turbulence. Physically, this can be caused by the effects of anisotropies, helicity, and/or shear. These large scale dynamos are amenable to mean field modeling (see below). On the other hand, small scale dynamo action is possible under fully isotropic conditions. This process has been studied both analytically and numerically; see Brandenburg & Subramanian (2005) for a review. Indeed, small scale dynamos tend to be quite prominent in simulations, perhaps more so than what is realistic. This may be a consequence of having used unrealistically large values of the magnetic Prandtl number, as will be discussed in the following.

The strength of the small scale dynamo depends significantly on the value of the magnetic Prandtl number  $\text{Pr}_M \equiv \nu/\eta$ , i.e. the ratio of the viscosity,  $\nu$ , to the magnetic diffusivity  $\eta$ . In the Sun,  $\text{Pr}_M$  varies between  $10^{-7}$  and  $10^{-4}$  between the top and the bottom of the convection zone, but it is always well below unity. In this case the Kolmogorov cutoff scale of the kinetic energy spectrum of the turbulence is much smaller than the resistive cutoff scale of the magnetic energy spectrum. Therefore, at the resistive scale where the small scale dynamo would operate fastest, the velocity is still in its inertial range where the spatial variation of the velocity is much more pronounced than it would be near the Kolmogorov scale, relevant for a magnetic Prandtl number of order unity. This tends to inhibit small scale dynamo action. In many simulations  $\text{Pr}_M$  is close to unity, because otherwise the



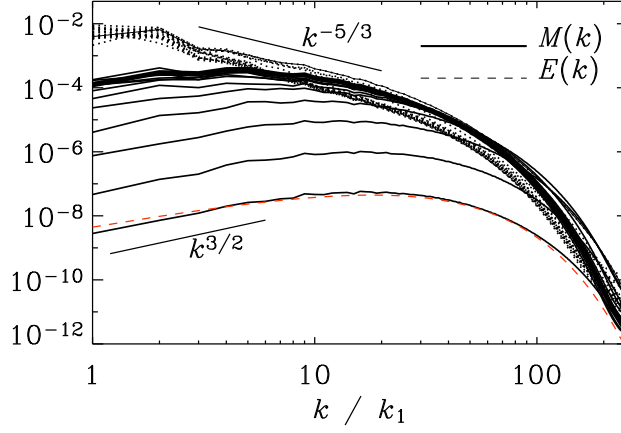


**Fig. 9.** Magnetic and kinetic energy spectra from a nonhelical turbulence simulation with  $P_m = 1$ . The kinetic energy is indicated as a dashed line (except for the first time displayed where it is shown as a thin solid line). At early times the magnetic energy spectrum follows the  $k^{3/2}$  Kazantsev (1968) law (the dashed line gives the fit to the analytic spectrum), while the kinetic energy shows a short  $k^{-5/3}$  range. The Reynolds number is  $u_{\text{rms}}/(\nu k_f) \approx 600$  and  $512^3$  meshpoints were used. The time difference between the spectra is about  $14 (k_f u_{\text{rms}})^{-1}$ . [Adapted from Brandenburg & Subramanian (2005).]

magnetic Reynolds number would be too small for the dynamo to be excited. As a consequence, the production of small scale field may be exaggerated in simulations. It is therefore possible that in the Sun small scale dynamo action is less important, and that large scale dynamo action is by comparison much more prominent, than found in simulations. An example may be the simulations of Brun et al. (2004), which are currently the highest resolution turbulence simulations of solar-like convection in spherical shell geometry. Here the magnetic field is indeed mostly of small scale.

In mean field models only the large scale field is modeled. This large scale field is governed both by turbulent magnetic diffusion as well as non-diffusive contributions such as the famous  $\alpha$  effect. As will be explained in the next section, this means that the mean electromotive force has a component parallel to the mean field, so it has a term of the form  $\alpha \overline{\mathbf{B}}$ ; see Brandenburg & Subramanian (2005) for a recent review. However, once a large scale field is present, the turbulent motions (which are always present) will wind up and mix the large scale field and will hence also produce a small scale field. This does *not* represent small scale dynamo action, even though there is a small scale field; if the large scale field is absent, the small scale field disappears.

Let us emphasize again that the Sun does possess a large scale field, with spatio-temporal order, as is evidenced by Figure 8. This automatically implies a small scale field. In addition, there may be small scale dynamo action occurring locally in the near-surface layers where the Coriolis force is comparatively weak, but this depends on whether or not small scale dynamo action is inhibited by a small value of the magnetic Prandtl number.

### 5.3 Mean field theory

The mean field approach allows the complicated three-dimensional dynamics to be treated in a statistical manner. The averaged equations are then only two-dimensional. In some cases, e.g. in Cartesian geometry, it can be useful to define two-dimensional averages, so that the resulting mean field equations are only one-dimensional. In the following we describe the essential features of this approach. By averaging the induction equation (45), e.g. according to the toroidal averaging procedure, we obtain

$$\frac{\partial \overline{\mathbf{B}}}{\partial t} = \nabla \times (\overline{\mathbf{U}} \times \overline{\mathbf{B}} + \overline{\mathcal{E}} - \eta \mu_0 \overline{\mathbf{J}}), \quad (47)$$

where  $\overline{\mathcal{E}} = \overline{\mathbf{u} \times \mathbf{b}}$  is the mean electromotive force from the small scale magnetic and velocity fields, with  $\mathbf{u} = \mathbf{U} - \overline{\mathbf{U}}$  and  $\mathbf{b} = \mathbf{B} - \overline{\mathbf{B}}$  being the fluctuations, i.e. the deviations from the corresponding averages.

There are two quite different approaches to calculating  $\overline{\mathcal{E}}$  and its dependence on  $\overline{\mathbf{B}}$ . The first order smoothing approximation uses just the linearized evolution equation for  $\mathbf{b}$ , while the tau approximation uses also the linearized momentum equation together with a closure hypothesis for the higher order triple correlation terms. For references and historical aspects we refer to the review by Brandenburg & Subramanian (2005). Both approaches predict the presence of terms of the form

$$\overline{\mathcal{E}}_i = \alpha_{ip} \overline{B}_p + \eta_{ipl} \overline{B}_{p,l}, \quad (48)$$

where a comma denotes partial differentiation. The tau approximation gives

$$\alpha_{ip} = -\tau \epsilon_{ijk} \overline{u_k u_{j,p}} + \tau \epsilon_{ijk} \overline{b_k b_{j,p}} / \rho_0, \quad (49)$$

where  $\tau$  is the correlation time. However, within the first order smoothing approximation the magnetic term in  $\alpha_{ip}$  is absent. In order to illuminate the meaning of these tensors, it is useful to make the assumption of isotropy,  $\tilde{\alpha}_{ip} = \tilde{\alpha} \delta_{ip}$  and  $\tilde{\eta}_{ipl} = \tilde{\eta}_t \epsilon_{ipl}$ . This yields

$$\tilde{\alpha} = -\frac{1}{3} (\overline{\boldsymbol{\omega} \cdot \mathbf{u}} - \overline{\mathbf{j} \cdot \mathbf{b}} / \rho_0), \quad \tilde{\eta}_t = \frac{1}{3} \overline{u^2}, \quad (50)$$

where  $\boldsymbol{\omega} = \nabla \times \mathbf{u}$  is the small scale vorticity and  $\mathbf{j} = \nabla \times \mathbf{b} / \mu_0$  is the small scale current density. Thus,  $\tilde{\alpha}$  is proportional to the residual helicity, i.e. the

difference between kinetic and current helicities, and  $\eta_t$  is proportional to the mean square velocity.

Using a closure assumption for the triple correlations we have, under the assumption of isotropy, the important result

$$\alpha = -\frac{1}{3}\tau (\overline{\boldsymbol{\omega} \cdot \mathbf{u}} - \overline{\mathbf{j} \cdot \mathbf{b}}/\rho_0), \quad \eta_t = \frac{1}{3}\tau \overline{u^2}. \quad (51)$$

The electromotive force takes then the form

$$\overline{\boldsymbol{\mathcal{E}}} = \alpha \overline{\mathbf{B}} - \eta_t \mu_0 \overline{\mathbf{J}}. \quad (52)$$

This equation shows that the electromotive force does indeed have a component in the direction of the mean field (with coefficient  $\alpha$ ). The  $\eta_t$  term corresponds to a contribution of the electromotive force that is formally similar to the microscopic diffusion term,  $\eta \mu_0 \overline{\mathbf{J}}$ , in equation (47). Therefore one speaks also of the total magnetic diffusivity,  $\eta_T = \eta + \eta_t$ . The presence of the  $\alpha$  term, on the other hand, has no correspondence to the non-turbulent case, and it is this term that invalidates Cowling's anti-dynamo theorem for mean fields. Indeed, there are simple self-excited (exponentially growing) solutions already in a one-dimensional model (see below).

Equation (51) shows that the presence of an  $\alpha$  effect is closely linked to the presence of kinetic and/or current helicity, while turbulent magnetic diffusion is always present when there is a small scale turbulent velocity field. This shows immediately that just increasing the turbulence (without also increasing the helicity) tends to *diminish* turbulent mean field dynamo action, rather than enhancing it, as one might have thought.

The formalism discussed above does not address the production of kinetic helicity in the Sun. This can be calculated perturbatively by considering the effects of vertical density and turbulent intensity stratification and rotation. At lowest order one finds

$$\alpha_{\phi\phi} = -\frac{16}{15}\tau^2 u_{\text{rms}}^2 \boldsymbol{\Omega} \cdot \nabla \ln(\rho u_{\text{rms}}) + \dots \quad (53)$$

for the first term in equation (49). For details we refer to the reviews by Rüdiger & Hollerbach (2004) and Brandenburg & Subramanian (2005). The magnetic contribution to the  $\alpha$  effect proportional to  $\overline{\mathbf{j} \cdot \mathbf{b}}$  (in the isotropic case) still needs to be added to the right hand side of equation (53). This  $\overline{\mathbf{j} \cdot \mathbf{b}}$  contribution is mainly the result of the dynamo itself, which tends to build up small scale current helicity along with the large scale magnetic field. Thus, the value of  $\overline{\mathbf{j} \cdot \mathbf{b}}$  cannot be obtained independently of the actual solution to the dynamo problem.

#### 5.4 Numerical determination of $\alpha$

A simple way of determining  $\alpha$  numerically is by imposing a constant field of strength  $\mathbf{B}_0$  over a domain of simulated turbulence. Since the mean field is

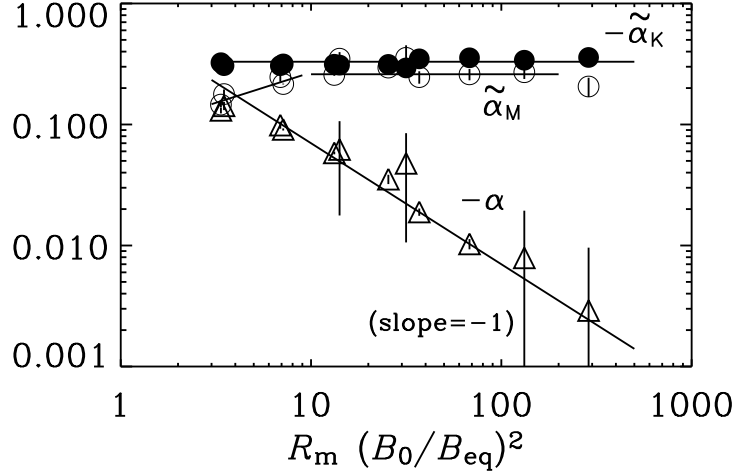


**Fig. 10.**  $R_m$  dependence of the normalized  $\alpha$  compared with dependence of  $\tilde{\alpha}_K^{(k)}$  for  $B_0/B_{eq}$  around unity. Vertical bars give error estimates. The vertical bars on the data points give estimates of the error (see text). [Adapted from Brandenburg & Subramanian (2005).]

constant, i.e.  $\overline{\mathbf{B}} = \mathbf{B}_0$ , the mean current density vanishes in equation (52), so  $\alpha$  can directly be determined by measuring the electromotive force,  $\overline{\mathbf{u} \times \mathbf{b}}$ , in the direction of the imposed field, and dividing one by the other. In other words,  $\alpha = \overline{\mathbf{u} \times \mathbf{b}} \cdot \mathbf{B}_0 / B_0^2$ . The values of  $\alpha$  collapse onto a single line. Looking at equation (51), such a decline of  $\alpha$  can only come about if either  $\tau$  or  $\overline{\boldsymbol{\omega} \cdot \mathbf{u}}$  decrease with  $B_0$ , or, alternatively, if  $\overline{\boldsymbol{\omega} \cdot \mathbf{u}}$  and  $\overline{\mathbf{j} \cdot \mathbf{b}}$  approach each other. It is quite clear from the data that neither  $\overline{\boldsymbol{\omega} \cdot \mathbf{u}}$  nor  $\tau$  decrease and that instead there is, at least for small values of  $R_m(B_0/B_{eq})^2$ , a tendency for  $\overline{\boldsymbol{\omega} \cdot \mathbf{u}}$  and  $\overline{\mathbf{j} \cdot \mathbf{b}}$  to approach one another.

The “catastrophic” decrease of  $\alpha$  with decreasing  $\eta$  is directly a consequence of magnetic helicity conservation in a closed or periodic domain, but this can be alleviated in the presence of helicity fluxes out of the domain. We return to this discussion in § 6.3 when we consider the consequences for the nonlinear saturation of the dynamo effect.

### 5.5 Other effects

There are a number of other effects that contribute to the algebraic relationship between the electromotive force and the mean field. One is a pumping effect associated with the antisymmetric components of the  $\alpha$  tensor,

$$\alpha_{ij}^{(A)} = \frac{1}{2}(\alpha_{ij} + \alpha_{ji}) \equiv -\frac{1}{2}\epsilon_{ijk}\gamma_k \quad (\text{pumping}), \quad (54)$$

where  $\gamma_k$  is the pumping velocity. This name is motivated by the fact that the term  $\alpha_{ij}^{(A)}\overline{B}_j$  can also be written as  $(\boldsymbol{\gamma} \times \overline{\mathbf{B}})_i$ . This shows that the vector  $\boldsymbol{\gamma}$  plays the role of an effective advection velocity.

The pumping effect is sometimes called turbulent diamagnetism. This has to do with a remarkable relation between pumping velocity and turbulent magnetic diffusion,

$$\boldsymbol{\gamma} = -\frac{1}{2}\nabla\eta_t. \quad (55)$$

Calculating the contribution to the electromotive force from this term together with the turbulent diffusion term gives

$$\overline{\boldsymbol{\mathcal{E}}} = \dots - \frac{1}{2}\nabla\eta_t \times \overline{\mathbf{B}} - \eta_t \nabla \times \overline{\mathbf{B}} = \dots - \frac{1}{\sigma_t} \nabla \times (\overline{\mathbf{B}}/\mu_t), \quad (56)$$

where

$$\sigma_t = \sigma(\eta_t/\eta)^{-1/2} \quad \text{and} \quad \mu_t = \mu_0(\eta_t/\eta)^{-1/2} \quad (57)$$

are turbulent conductivity and turbulent permeability, respectively. (The normalization with the microscopic values of  $\sigma$  and  $\mu_0$  is done in order for the turbulent values of  $\sigma_t$  and  $\mu_t$  to have correct dimensions.)

Another potentially important term is an effect of the form  $\boldsymbol{\delta} \times \overline{\mathbf{J}}$ , which has long been known to be able to produce dynamo action if its components are of the appropriate sign relative to the orientation of shear. It is clear that  $\boldsymbol{\delta}$  must be an axial vector, and both the local angular velocity,  $\boldsymbol{\Omega}$ , as well as the vorticity of the mean flow,  $\overline{\mathbf{W}} = \nabla \times \overline{\mathbf{U}}$  are known to contribute. Dynamo action is only possible when  $\boldsymbol{\delta}$  and  $\overline{\mathbf{W}}$  are antiparallel. It is still not quite clear from turbulence calculations whether the orientation of the vector  $\boldsymbol{\delta}$  relative to the shear is appropriate for dynamo action in the convection zone.

## 6 Models of the solar cycle

### 6.1 One-dimensional models

It has long been known that an  $\alpha$  effect combined with differential rotation can cause oscillatory propagating solutions. In order to appreciate the possibility of oscillatory self-excited solutions, let us consider one-dimensional solutions, allowing for variations only in the  $z$  direction, but field components still pointing in the two directions. Applied to the Sun, we may think of the  $z$  direction being latitude (= negative colatitude,  $-\theta$ ),  $x$  being radius, and  $y$  being longitude, so  $(x, y, z) \rightarrow (r, \phi, -\theta)$ . Let us consider a mean flow of the form  $\overline{\mathbf{U}} = (0, Sx, 0)$ , i.e. the flow has only a  $y$  component that varies linearly in the  $x$  direction. We write the field in the form  $\overline{\mathbf{B}}(z, t) = (-\overline{A}'_y, \overline{B}_y, 0)$ , where a prime denotes a  $z$  derivative. The corresponding dynamo equation can then be written as

$$\dot{\overline{A}}_y = \alpha \overline{B}_y + (\eta + \eta_t) \overline{A}_y'', \quad (58)$$

$$\dot{\overline{B}}_y = S \overline{B}_x + (\eta + \eta_t) \overline{B}_y'', \quad (59)$$

where we have neglected a term  $(\alpha \overline{B}_x)'$  in comparison with  $S \overline{B}_x$  in the second equation. (Here  $\overline{B}_x = -\overline{A}_y'$  is the radial field.)

Solutions to these equations are frequently discussed in the literature (e.g. Moffatt 1978, Brandenburg & Subramanian 2005). It is instructive to consider first solutions in an unbounded domain, e.g.  $0 < z < L_z$ , so the solutions are of the form

$$\overline{\mathbf{B}}(z, t) = \text{Re} \left[ \hat{\mathbf{B}}_{\mathbf{k}} \exp(ikz + \lambda t) \right]. \quad (60)$$

There are two physically meaningful solutions. Both have an oscillatory component, but one of them can also have an exponentially growing component such that real and imaginary parts of  $\lambda$  are given by

$$\text{Re} \lambda = -\eta_T k^2 + \left| \frac{1}{2} \alpha S k \right|^{1/2}, \quad (61)$$

$$\text{Im} \lambda \equiv -\omega_{\text{cyc}} = \left| \frac{1}{2} \alpha S k \right|^{1/2}. \quad (62)$$

The solutions are oscillatory with the cycle period  $\omega_{\text{cyc}}$ . This shows that, in the approximation where the  $(\alpha \overline{B}_x)'$  term is neglected (valid when  $Sk \gg \alpha$ ), the mean field dynamo is excited when the dynamo number,

$$D = \left| \frac{1}{2} \alpha S k \right|^{1/2} / (\eta_T k^2), \quad (63)$$

exceeds a critical value that is in this simple model  $D_{\text{crit}} = 1$ .

A number of important conclusions can be drawn based on this simple model. (i) The cycle frequency is proportional to  $\sqrt{\alpha S}$ , but becomes equal to  $\eta_T k^2$  in the marginal or nonlinearly saturated cases. (ii) There are dynamo waves with a pattern speed proportional to  $\eta_T k$  propagating along contours of constant shear. For example, for radial angular velocity contours with angular velocity decreasing outwards, and for a positive  $\alpha$  in the northern hemisphere, the propagation is equatorward. If the sign of either  $S$  or  $\alpha$  is reversed, the propagation direction is reversed too.

For more realistic applications to the Sun one must solve the mean field dynamo equations in at least two dimensions over a spherical domain with appropriate profiles for  $\alpha$ ,  $\eta_T$ , and  $\Omega$ . In the following we discuss four different dynamo scenarios that have been studied over the years.

If the flow is assumed given, no feedback via the Lorentz force is allowed, so the dynamo equations are linear and the magnetic energy would eventually grow beyond all bounds. In reality, the magnetic field will affect the flow and hence  $\overline{\mathbf{U}}$ , as well as  $\alpha$ ,  $\eta_t$ , and other turbulent transport coefficients will be affected. We will postpone the discussion of the nonlinear behavior to §6.3.

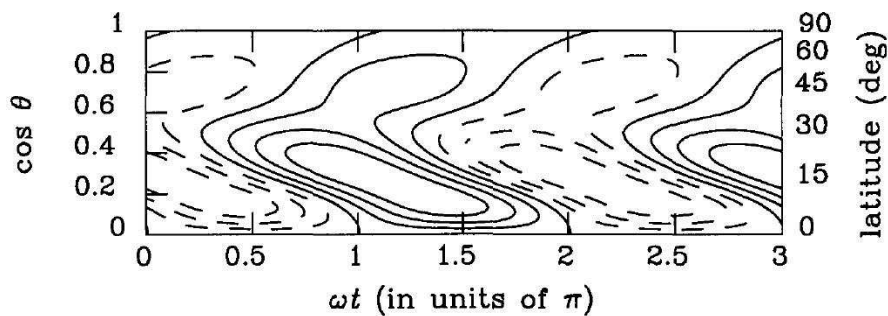


**Fig. 11.** Butterfly diagram of  $B_\phi$  taken at reference depth  $r = 0.85R_\odot$ . [Adapted from Brandenburg & Tuominen (1988).]

## 6.2 Different solar dynamo scenarios

A traditional and also quite natural approach is to calculate the profiles for  $\alpha$  and  $\eta_t$  using the results from mean field theory such as equation (53) and to take the profiles for the rms velocity and the correlation time,  $\tau = \ell/u_{\text{rms}}$ , from stellar mixing length models using  $\ell = \alpha_{\text{mix}}H_p$  for the mixing length, where  $H_p$  is the pressure scale height. For  $\Omega(r, \theta)$  one often uses results from helioseismology. In Figure 11 we reproduce the results of an early paper where the  $\Omega(r, \theta)$  profile was synthesized from a collection of different helioseismology results then available. The  $\alpha$  and  $\eta_t$  profiles, as well as profiles describing some other effects (such as pumping and  $\mathbf{\Omega} \times \mathbf{\bar{T}}$  effects) were taken from a solar mixing length model. In this model an equatorward migration is achieved in a limited range in radius where  $\partial\Omega/\partial r < 0$ . In this model this is around  $r = 0.8R_\odot$ . Note also that in this case  $\bar{B}_r$  and  $\bar{B}_\phi$  are approximately in antiphase, as is also seen in the Sun.

Distributed dynamos have been criticized on the grounds that magnetic buoyancy will rapidly remove the magnetic field from the convection zone. Since then, helioseismology has shown that the radial  $\Omega$  gradient is virtually zero in the bulk of the convection zone and only at the bottom is there a finite gradient, but it is positive at latitudes below  $\pm 30^\circ$ . This may still yield an equatorward migration in the butterfly diagram, because equation (53) would predict that at the bottom of the convection zone, where the magnitude of the positive  $\nabla_r \ln u_{\text{rms}}$  gradient exceeds that of the negative  $\nabla_r \ln \rho$  gradient. This changes the sign of  $\alpha$ , and makes it negative near the bottom of the convection zone in the northern hemisphere. This led to the idea of the overshoot dynamo that is believed to operate only in a thin layer at or just below the convection zone proper. Such dynamos have been considered by a number of different groups.

In Figure 12 we show the result of an overshoot dynamo calculation. An important problem that emerges from such an approach is that when the dynamo layer is too thin, the toroidal flux belts are too close to each other

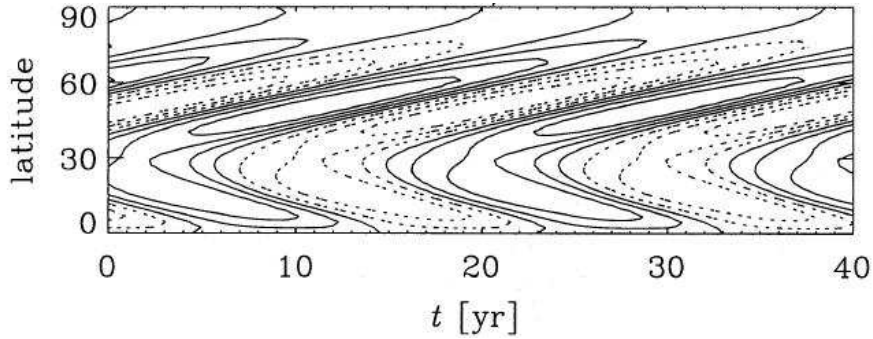


**Fig. 12.** Butterfly diagram of  $B_\phi$  evaluated at the bottom of the convection zone at  $r = 0.7R_\odot$ . [Adapted from Rüdiger & Brandenburg (1995).]

in latitude. This leads to the conclusion that the thickness of the dynamo region should not be less than 35 Mm. At the bottom of the convection zone this corresponds to half a pressure scale height. However, this value is already rather large and no longer supported by helioseismology, which predicts the thickness of the overshoot layer to be about 7 Mm or less.

Another variant of this approach is the interface dynamo. The main difference here is that  $\alpha$  is assumed to operate in the bulk of the convection zone, but it is still taken to be negative, so as to give equatorward migration. Also important is the sharp jump in  $\eta_t$  at the bottom of the convection zone. However, when the latitudinal variation of the angular velocity is included, no satisfactory butterfly diagram is obtained.

A completely different class of dynamos are the flux transport dynamos that are governed by the effect of meridional circulation transporting surface flux to the poles and flux along the tachocline toward the equator. The  $\alpha$  effect is now assumed positive, so in the absence of meridional circulation the dynamo wave would propagate poleward. However, under certain conditions, meridional circulation can actually reverse the direction of propagation of the dynamo wave. A calculation with a realistic solar angular velocity profile has been presented by Dikpati & Charbonneau (1999); see Figure 13. They establish a detailed scaling law for the dependence of the cycle period on the circulation speed, the  $\alpha$  effect (or source term), and the turbulent magnetic diffusivity. To a good approximation they find the cycle period to be inversely proportional to the circulation speed.

With such a variety of different models and assumptions (most of them ignoring what was previously derived for  $\alpha(r, \theta)$ ,  $\eta_t(r, \theta)$ , and other transport effects), dynamo theory has been perceived as rather arbitrary. One reason for this level of arbitrariness that developed in modeling the solar dynamo is that the effects of nonlinearity are not well understood. This might affect the properties of the dynamo coefficients in the saturated state making



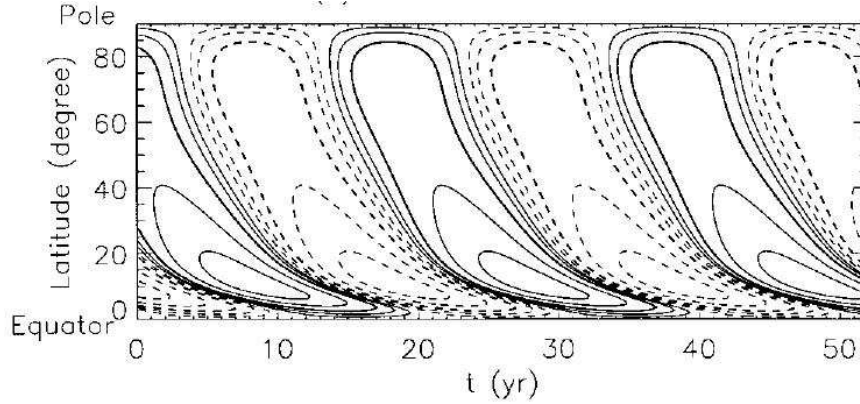


**Fig. 13.** Butterfly diagram of  $B_\phi$  at  $r = 0.7R_\odot$ . The maximum circulation speed at the surface is  $15 \text{ ms}^{-1}$  and the turbulent magnetic diffusivity is assumed to be  $\eta_t = 3 \times 10^{11} \text{ cm}^2 \text{ s}^{-1}$ . [Courtesy of Dikpati & Charbonneau (1999).]

them quite different from those obtained in linear theory. In the following we sketch briefly the tremendous developments on nonlinear saturation that have occurred in the past few years.

### 6.3 Nonlinear saturation

The effects of nonlinearity can be divided into macroscopic and microscopic effects. The former is simply the result of  $\overline{\mathbf{B}}$  on  $\overline{\mathbf{U}}$ , as described by the Lorentz force,  $\overline{\mathbf{J}} \times \overline{\mathbf{B}}$ , in the mean field momentum equation. This effect is sometimes also referred to as the Malkus–Proctor effect and has been incorporated to various degree of sophistication in a number of models starting with incompressible models in the context of the geodynamo and the solar dynamo.

The microscopic feedback can be subdivided into two different contributions. The effect of  $\overline{\mathbf{B}}$  on the turbulent velocity (conventional  $\alpha$  quenching), and the more direct effect of the small scale current helicity,  $\overline{\mathbf{j} \cdot \mathbf{b}}$  (or  $\epsilon_{ijk} \overline{b_k b_{j,p}}$  in the anisotropic case), on the  $\alpha$  effect or, more precisely, on the electromotive force. The latter can, under some conditions, lead to catastrophic  $\alpha$  quenching; see Brandenburg & Subramanian (2005) for a review of this vast field of recent research.

The  $\overline{\mathbf{j} \cdot \mathbf{b}}$  term cannot be implemented directly, because it is necessary to have a theory for how  $\overline{\mathbf{j} \cdot \mathbf{b}}$  depends on the mean field. Under some idealized conditions (steady state, triply-periodic boundary conditions) the answer can be obtained from the general evolution equation for magnetic helicity, which reads

$$\frac{\partial}{\partial t}(\mathbf{A} \cdot \mathbf{B}) + \nabla \cdot \mathcal{F}_H = -2\eta\mu_0(\mathbf{J} \cdot \mathbf{B}). \quad (64)$$

Here,  $\mathbf{A}$  is the magnetic vector potential with  $\mathbf{B} = \nabla \times \mathbf{A}$ , while  $\mathbf{A} \cdot \mathbf{B}$  is the magnetic helicity density, and  $\mathcal{F}_H$  is its flux. Magnetic helicity and its flux are gauge-dependent, i.e. they are not invariant under the transformation  $\mathbf{A} \rightarrow \mathbf{A}' = \mathbf{A} + \nabla \Lambda$ . However, when averaging over a triply-periodic volume this ambiguity disappears and  $\langle \mathbf{A} \cdot \mathbf{B} \rangle$  is gauge-invariant and obeys

$$\frac{d}{dt} \langle \mathbf{A} \cdot \mathbf{B} \rangle = -2\eta\mu_0 \langle \mathbf{J} \cdot \mathbf{B} \rangle. \quad (65)$$

(The spatial average of a divergence also vanishes for triply periodic domains.) We see that in the steady state,  $d/dt = 0$ , so  $\langle \mathbf{J} \cdot \mathbf{B} \rangle = 0$ . Splitting into large scale and small scale contributions, we have  $\langle \mathbf{j} \cdot \mathbf{b} \rangle = -\langle \bar{\mathbf{J}} \cdot \bar{\mathbf{B}} \rangle$ . This connects the small scale current helicity explicitly with the properties of the large scale field.

The same procedure can still be applied in the unsteady case by considering magnetic helicity evolution for the large scale and small scale components, i.e. for  $\langle \bar{\mathbf{A}} \cdot \bar{\mathbf{B}} \rangle$  and  $\langle \mathbf{a} \cdot \mathbf{b} \rangle$ . The evolution of  $\langle \bar{\mathbf{A}} \cdot \bar{\mathbf{B}} \rangle$  follows straightforwardly from the mean field equations, which shows that there is continuous production of large scale magnetic helicity given by  $2\bar{\mathcal{E}} \cdot \bar{\mathbf{B}}$ . In order not to produce any net magnetic helicity, as required by equation (65), the evolution of  $\langle \mathbf{a} \cdot \mathbf{b} \rangle$  has the same term but with the opposite sign. Furthermore, under isotropic conditions,  $\langle \mathbf{a} \cdot \mathbf{b} \rangle$  is proportional to  $\langle \mathbf{j} \cdot \mathbf{b} \rangle$ , which in turn is proportional to the magnetic contribution to the  $\alpha$  effect. Finally, the restriction to triply periodic boundary conditions can be relaxed (and hence a flux divergence can be permitted) if there is sufficient scale separation, i.e. if the energy carrying scale of the turbulence is clearly smaller than the domain size.

This then leads to an explicit evolution equation for the magnetic  $\alpha$  effect,

$$\frac{\partial \alpha_M}{\partial t} + \nabla \cdot \bar{\mathcal{F}}_\alpha = -2\eta_t k_f^2 \left( \frac{\bar{\mathcal{E}} \cdot \bar{\mathbf{B}}}{B_{\text{eq}}^2} + \frac{\alpha_M}{R_m} \right), \quad (66)$$

where  $\alpha_M = \frac{1}{3}\tau \overline{\mathbf{j} \cdot \mathbf{b}}$  is the magnetic  $\alpha$  effect and  $\bar{\mathcal{F}}_\alpha = \frac{1}{3}\tau \bar{\mathcal{F}}_C$ , where  $\bar{\mathcal{F}}_C \approx k_f^2 \bar{\mathcal{F}}_H$  is the current helicity flux. This so-called dynamical  $\alpha$  quenching equation is able to reproduce the resistively slow saturation behavior, found in simulations of helically driven turbulence. In the steady state, this equation predicts for  $\alpha = \alpha_K + \alpha_M$

$$\alpha = \frac{\alpha_K + R_m (\eta_t \bar{\mathbf{J}} \cdot \bar{\mathbf{B}} + \nabla \cdot \bar{\mathcal{F}}_\alpha)}{1 + R_m \bar{\mathbf{B}}^2 / B_{\text{eq}}^2}. \quad (67)$$

Note that in the special case of periodic domains, used in some simulations where  $\bar{\mathbf{J}} = \mathbf{0}$  and  $\nabla \cdot \bar{\mathcal{F}}_\alpha = 0$ , this equation predicts catastrophic quenching, i.e.  $\alpha = \alpha_K / (1 + R_m \bar{\mathbf{B}}^2 / B_{\text{eq}}^2)$ , so  $\alpha$  is suppressed relative to its kinematic value  $\alpha_K$  in a strongly Reynolds number-dependent fashion—as seen in Figure 10.

In the case of open boundaries, there is a flux of magnetic helicity. Under the two-scale hypothesis this can be defined in a gauge-invariant manner.

Magnetic helicity fluxes provide a way to escape the otherwise resistively limited saturation and catastrophic quenching. Several simulations and mean field models have confirmed this. Although dynamical quenching has already been applied to solar dynamo models it remains to be seen to what extent the previously discussed conclusions about distributed versus overshoot layer dynamos are affected, and what the role of meridional circulation is in such a model.

## 6.4 Location of the dynamo

It is generally believed that the magnetic field emergence in the form of sunspots is deeply rooted and associated with strong toroidal flux tubes of strength up to 100 kG, as predicted by the so-called thin flux tube models. When parts of the flux tube become destabilized due to magnetic buoyancy, it rises to the surface to form a sunspot pair. However, there are some open questions: how are such coherent tubes generated and what prevents them from breaking up during the ascent over 20 pressure scale heights? Alternatively, the usual mean field dynamo would actually predict magnetic field generation distributed over the entire convection zone. Sunspot formation would mainly be associated with local flux concentration within regions of enhanced net flux. This picture is appealing in many ways and has been discussed in more detail in Brandenburg (2005). However, although both pictures (deep rooted versus distributed dynamo) have received some support from mean field modeling, there is still no global turbulence simulations that reproduces the solar activity cycle without questionable assumptions.

# 7 Differential rotation

It became clear from the discussion in §6 that differential rotation plays an important role in producing a large scale magnetic field in the Sun. It may also be important for the dynamo in disposing of its excess small scale current helicity, as discussed in the previous section. In this section we discuss the theoretical basis for explaining the origin and properties of solar and stellar differential rotation.

## 7.1 Mean field theory of differential rotation

The origin of differential rotation has long been understood to be a consequence of the anisotropy of convection. It has long been clear that the vertical exchange of momentum by convection should lead to a tendency toward constant angular momentum in the radial direction, i.e.  $\overline{\Omega}\varpi^2 = \text{const}$ , and hence the mean angular velocity scales with radius like  $\overline{\Omega}(r) \sim r^{-2}$ . Here,  $\varpi = r \sin \theta$  denotes the cylindrical radius (i.e. the distance from the rotation axis).

The  $r\phi$  component of the viscous stress tensor contributes to the angular momentum equation,

$$\frac{\partial}{\partial t} (\rho \varpi^2 \overline{\Omega}) + \nabla \cdot [\rho \varpi (\overline{\mathbf{U}} \overline{U}_\phi + \overline{\mathbf{u} u_\phi})] = 0, \quad (68)$$

where  $\overline{u_i u_j} = Q_{ij}$  are the components of the Reynolds tensor. In spherical coordinates the full mean velocity vector is written as  $\overline{\mathbf{U}} = (\overline{U}_\varpi, \varpi \overline{\Omega}, \overline{U}_z)$ .

The early treatment in terms of an anisotropic viscosity tensor was purely phenomenological. A rigorous calculation of the Reynolds stresses shows that the mean Reynolds stress tensor is described not only by diffusive components that are proportional to the components of the rate of strain tensor of the mean flow, but that there are also non-diffusive components that are directly proportional to the local angular velocity. In particular the  $r\phi$  and  $\theta\phi$  components of the Reynolds tensor are of interest for driving  $r$  and  $\theta$  gradients of  $\overline{U}_\phi \equiv \varpi \overline{\Omega}$ . Thus, for ordinary isotropic turbulent viscosity one has, using Cartesian index notation,

$$Q_{ij} = -\nu_t (\overline{U}_{i,j} + \overline{U}_{j,i}) - \zeta_t \delta_{ij} \overline{U}_{k,k}, \quad (69)$$

where  $\zeta_t$  is a turbulent bulk viscosity, and commas denote partial differentiation. This expression implies in particular that

$$Q_{\theta\phi} = -\nu_t \sin \theta \frac{\partial \overline{\Omega}}{\partial \theta}. \quad (70)$$

Note that for the Sun, where  $\partial \overline{\Omega} / \partial \theta > 0$  in the northern hemisphere, this formula would predict that  $Q_{\theta\phi}$  is negative in the northern hemisphere. However, it was noted long ago from correlation measurements of sunspot proper motions that  $Q_{\theta\phi}$  is in fact *positive* in the northern hemisphere. The observed profile of  $Q_{\theta\phi}$  is also known as the Ward profile. The observed positive sign was used to motivate that there must be an additional term in the expression for  $Q_{ij}$ . Using a closure approach, such as the first order smoothing approximation that is often used to calculate the  $\alpha$  effect in dynamo theory, one can find the coefficients in the expansion

$$Q_{ij} = \Lambda_{ijk} \overline{\Omega}_k - \mathcal{N}_{ijkl} \overline{U}_{k,l}, \quad (71)$$

where  $\Lambda_{ijk}$  describes the so-called  $\Lambda$  effect and  $\mathcal{N}_{ijkl}$  is the turbulent viscosity tensor. The viscosity tensor  $\mathcal{N}_{ijkl}$  must in general be anisotropic. When anisotropies are included,  $\mathcal{N}_{ijkl}$  gets modified (but it retains its overall diffusive properties), and  $\Lambda_{ijk}$  takes the form

$$\Lambda_{ijk} \overline{\Omega}_k = \begin{pmatrix} 0 & 0 & V \sin \theta \\ 0 & 0 & H \cos \theta \\ V \sin \theta & H \cos \theta & 0 \end{pmatrix} \overline{\Omega}, \quad (72)$$

where  $V$  and  $H$  are still functions of radius, latitude, and time;  $V$  is thought to be responsible for driving vertical differential rotation ( $\partial\overline{\Omega}/\partial r \neq 0$ ) while  $H$  is responsible for latitudinal differential rotation ( $\partial\overline{\Omega}/\partial\theta \neq 0$ ).

The first order smoothing approximation predicts the following useful approximations for  $V$  and  $H$ :

$$V \approx \tau \left( \overline{u_\phi^2} - \overline{u_r^2} \right), \quad (73)$$

$$H \approx \tau \left( \overline{u_\phi^2} - \overline{u_\theta^2} \right). \quad (74)$$

These expressions show that when the rms velocity in the radial direction is larger than in the azimuthal direction we must expect  $V < 0$  and hence  $\partial\overline{\Omega}/\partial r < 0$ . In the Sun, this effect is responsible for the negative radial shear near the surface where strong downdrafts may be responsible for a comparatively large value of  $\overline{u_r^2}$ . Likewise, when the rms velocity in the latitudinal direction is larger than in the azimuthal direction we expect  $H < 0$  and hence  $\partial\overline{\Omega}/\partial\theta < 0$ , so the equator would spin slower than the poles. This does not apply to the Sun, but it may be the case in some stars, especially when the flows are dominated by large scale meridional circulation.

## 7.2 The $A$ effect from turbulence simulations

Several of the relationships described above have been tested using convection simulations, both in local Cartesian boxes located at different latitudes as well as in global spherical shells. Generally, the various simulations agree in that the sign of the horizontal Reynolds stress is positive in the northern hemisphere and negative in the southern, reproducing thus the Ward profile. The simulations also show that the off-diagonal components of the turbulent heat transport tensor are mostly positive in the northern hemisphere, and negative in the southern hemisphere. This agrees with the sign required if the baroclinic term is to produce a tendency toward spoke-like angular velocity contours. Simulations also reproduce the sudden drop of angular velocity at the top of the convection zone. This agrees with a predominantly negative sign of the vertical Reynolds stress at a similar depth. Furthermore, some of the more recent simulations show an unexpectedly sharp increase of the horizontal Reynolds stress just near the equator (at around  $\pm 5^\circ$  latitude), before changing sign right at the equator. The significance of this result for the solar differential rotation pattern is still unclear.

## 7.3 Meridional flow and the baroclinic term

According to the formalism described in the previous section, a finite differential rotation can be obtained by ignoring meridional flows and solving equation (68) in isolation. However, this would only be a poor approximation

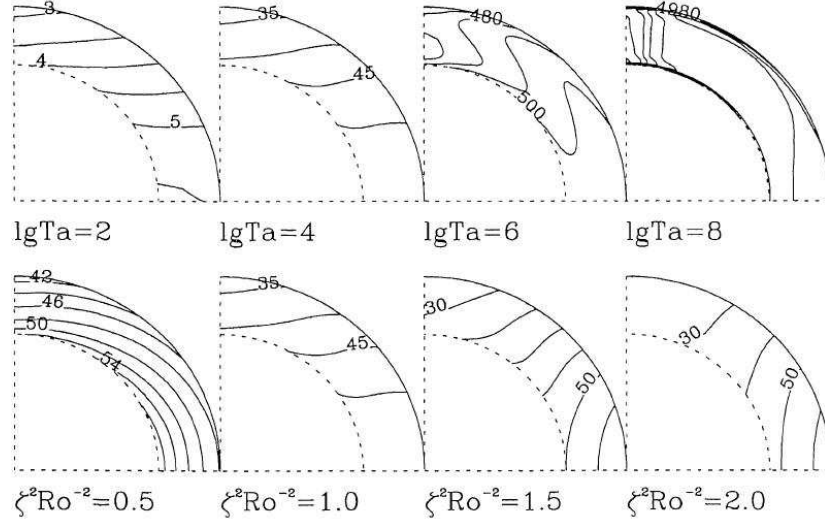


**Fig. 14.** Contours of constant  $\overline{\Omega}$  for different values of Taylor number (upper panel) and different values of the inverse Rossby number, affecting the relative importance of  $H$  over  $V$  (lower panel). [Adapted from Brandenburg et al. (1990).]

that becomes quickly invalid when the angular velocity becomes large compared with the turbulent viscous decay rate. This is quantified by the Taylor number

$$Ta = (2\overline{\Omega}_0 R^2 / \nu_t)^2. \quad (75)$$

Using the first order smoothing expression from Rüdiger (1989),  $\nu_t = (2/15) \tau u_{\text{rms}}^2$ , we have for values typical for the Sun (see Table 1), i.e.  $\nu_t \approx 10^{12} \text{cm}^2/\text{s}$ ,  $Ta \approx 10^9$ . This value of  $Ta$  is rather large so that nonlinearities produce strong deviations from linear theory.

As the value of  $Ta$  is increased, the Coriolis force increases, which then drives a meridional flow. This meridional flow first increases with increasing values of  $Ta$ , but then it reaches a maximum at  $Ta \approx 3 \times 10^5$ , and later declines with increasing values of  $Ta$ . (The solar value is  $Ta \approx 3 \times 10^7$ .) This decline is because eventually the Coriolis force can no longer be balanced against advection or diffusion terms. This can best be seen by considering the curl of the momentum equation,

$$\frac{\partial \overline{W}_\phi}{\partial t} + \varpi \overline{U} \cdot \nabla \left( \frac{\overline{W}_\phi}{\varpi} \right) - \nu_t D^2 \overline{W}_\phi = \varpi \frac{\partial \overline{\Omega}^2}{\partial z} + \hat{\phi} \cdot \nabla T \times \nabla S. \quad (76)$$

We recall that we consider here a nonrotating frame of reference, so there is no Coriolis force. Nevertheless, part of the inertial term takes a form that is

quite similar to the Coriolis term, but here  $\overline{\Omega}$  is a function of position, while in the Coriolis term the angular velocity would normally be a constant.

In the barotropic case one has  $\nabla T \parallel \nabla S$  so there is no baroclinic term, i.e.  $\hat{\phi} \cdot (\nabla T \times \nabla S) = 0$ . So, if viscous and inertial terms are small, which is indeed the case for rapid rotation, then  $\partial \overline{\Omega}^2 / \partial z$  has to vanish, so  $\overline{\Omega}$  would be constant along cylinders; see Figure 14. It is generally believed that the main reason for  $\overline{\Omega}$  not having cylindrical contours in the Sun is connected with the presence of the baroclinic term. The presence of magnetic forces may also play a role, but unlike the baroclinic term, magnetic forces tend to produce a rather variable  $\overline{\Omega}$  patterns, often connected with rapid motions near the poles where the inertia is lower.

Currently the highest resolution simulations of global convection in spherical shells are those by Miesch et al. (2000). These simulations show a great amount of detail and reproduce some basic features of the Sun's differential rotation such as the more rapidly spinning equator. However, in low latitudes they show strongly cylindrical  $\overline{\Omega}$  contours that deviate markedly from the more spoke-like contours inferred for the Sun using helioseismology. These simulations also do not show the near-surface shear layer where the rotation rate drops by over 20 nHz over the last 30 Mm below the surface.

Mean field simulations using the  $\Lambda$  effect show surprisingly good agreement with the helioseismologically inferred  $\overline{\Omega}$  pattern, and they are also beginning to address the problem of the near-surface shear layer. In these simulations it is indeed the baroclinic term that is responsible for causing the departure from cylindrical contours. This, in turn, is caused by an anisotropy of the turbulent heat conductivity which causes a slight enhancement in temperature and entropy at the poles. In the bulk of the convection zone the entropy is nearly constant, so the radial entropy variation is smallest compared with the radial temperature variation. It is therefore primarily the latitudinal entropy variation that determines the baroclinic term, with

$$\varpi \frac{\partial \overline{\Omega}^2}{\partial z} \approx -\hat{\phi} \cdot \overline{\nabla T \times \nabla S} \approx -\frac{1}{r} \frac{\partial \overline{T}}{\partial r} \frac{\partial \overline{S}}{\partial \theta} < 0. \quad (77)$$

The inequality shows that negative values of  $\partial \overline{\Omega}^2 / \partial z$  require that the pole is slightly warmer than the equator ( $\partial \overline{S} / \partial \theta < 0$ ). However, this effect is so weak that it cannot at present be observed. Allowing for these conditions in a simulation may require particular care in the treatment of the outer boundary conditions. In Figure 15 we show the plots of angular velocity contours and convective energy transport in a model with anisotropic turbulent conductivity tensor,  $\chi_{ij}$ . Given that the flux,  $\mathbf{F}$ , is proportional to  $-\chi_{ij} \nabla_j \overline{S}$ , a negative  $\partial \overline{S} / \partial \theta$  can be produced from a positive  $F_r$  with a positive value of  $\chi_{r\theta}$ .

In the discussion above we ignored in the last step a possible correlation between entropy and temperature fluctuations, i.e. a contribution from the term  $\overline{\nabla T' \times \nabla S'}$  where primes denote fluctuations. Such correlations, if of

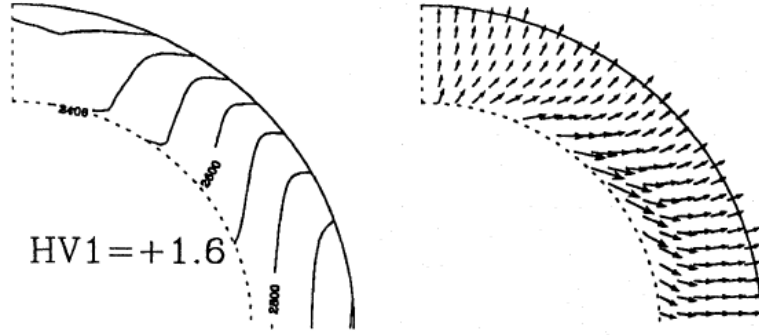


**Fig. 15.** Contours of angular velocity (left) and turbulent convective energy flux (right) for a model with anisotropic heat transfer tensor. [Adapted from Brandenburg et al. (1992).]

suitable sign, might provide yet a further explanation for a non-zero value of  $\partial \overline{\Omega}^2 / \partial z$ .

#### 7.4 Near-surface shear layer

The first results of helioseismology indicated significantly higher angular velocities in the sub-surface than what is seen at the surface using Doppler measurements. This apparent conflict is now resolved in that helioseismological inversions of the data from the SOHO spacecraft show a sharp negative gradient, connecting the observed surface values smoothly with the local maximum of the angular velocity at about 35 Mm depth; see Figure 16.

The theory of this negative near-surface shear layer is still a matter of ongoing research, but it is clear that negative shear would generally be the result of predominantly vertical turbulent velocities such as strong downdrafts near the radiating surface. However, such a layer that is dominated by strong downdrafts was only thought to be several megameters deep, and not several tens of megameters. With an improved theory for the anisotropy of the turbulence especially near the surface layers, one obtains a clear radial decline of the local angular velocity near the surface, although still not quite as much as is observed; see Figure 17. In any case, these results do at least reproduce the near-surface shear layer qualitatively correctly. A proper understanding of this layer is now quite timely in view of the fact that near-surface shear is likely to contribute to the production of strong toroidal fields.

#### 7.5 Magnetic effects

In § 4.5 we mentioned the torsional oscillations, which is a cyclic modulation of the latitudinal profile of the angular velocity at the surface of the sun.



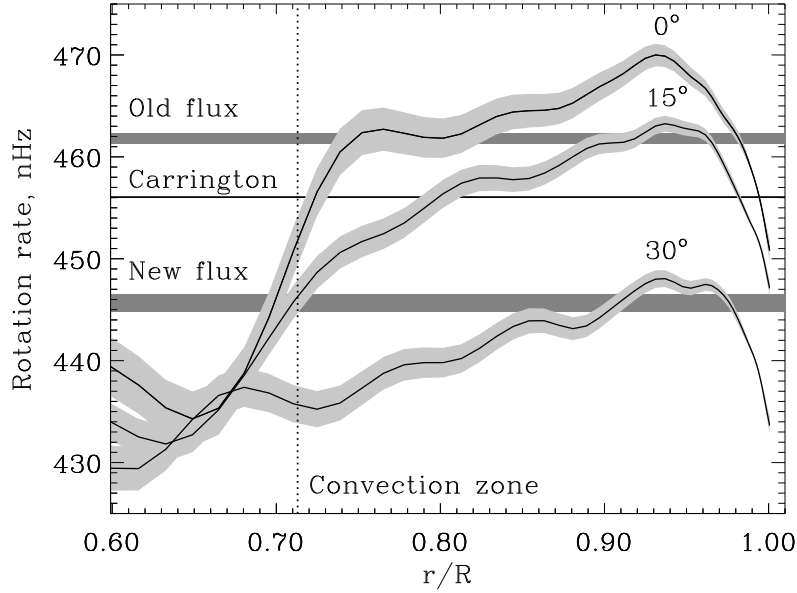


**Fig. 16.** Radial profiles of the internal solar rotation rate, as inferred from helioseismology (sidereal, i.e. in a fixed frame). The rotation rate of active zones at the beginning of the cycle (at  $\approx 30^\circ$  latitude) and near the end (at  $\approx 4^\circ$ ) is indicated by horizontal bars, which intersect the profiles of rotation rate at  $r/R_\odot \approx 0.97$ . For orientation, the conventionally defined Carrington rotation period of 27.3 days (synodic value, corresponding to 424 nHz) has been translated to the sidereal value of 456 nHz. Courtesy of Benevolenskaya et al. (1999).

Model calculations suggest that these oscillations can well be modeled by restoring the Lorentz force by adding a term  $-\varpi \overline{\mathbf{B}} \overline{\mathbf{B}}_\phi$  under the divergence in equation (68). Unfortunately, given that there is no definitive solar dynamo model, models for the Sun's torsional oscillations are equally preliminary and still a matter ongoing research.

In this connection it may be worth noting that there are also magnetic effects on other properties of the sun, most notably luminosity variations (by about 0.1%) and changes of the Sun's quadrupole moment. The latter does not really seem to be important for the Sun, but in close binaries this effect leads to measurable changes in the orbital period.

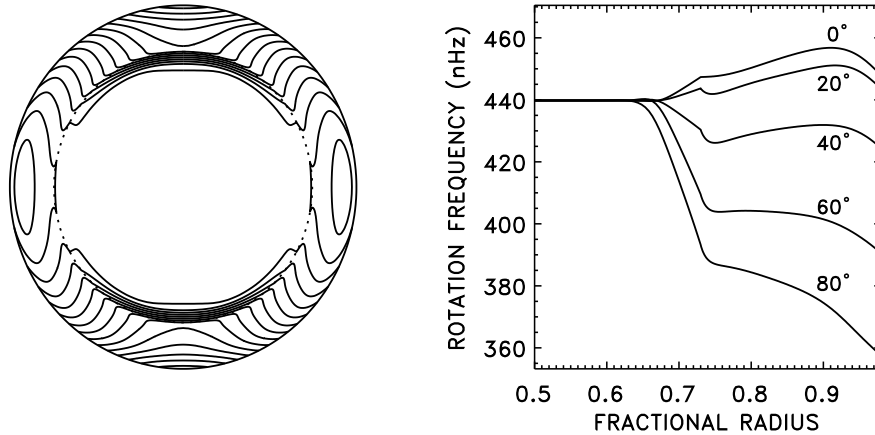


**Fig. 17.** Rotation law obtained by Kitchatinov & Rüdiger (2005) taking the anisotropy of the turbulence near the surface into account. [Courtesy Kitchatinov & Rüdiger (2005).]

## 8 Conclusions

In the past few decades there have been significant developments in understanding the physics of the Sun. Even regarding the radial structure of the Sun, which was thought to be qualitatively well understood, major revisions have emerged just recently with the refinement of three-dimensional simulations of solar granulation. Such simulations have led to new spectral line fits that imply a drastically reduced abundance of the heavier elements. This has consequences for the opacities that affect the deep parts of the Sun's interior.

There are many aspects of solar physics where a detailed understanding of the three-dimensional flow pattern of the Sun is crucial. It is not surprising that effects involving details of the turbulent flow field in the solar convection zone, such as the theory of differential rotation and magnetic field generation, provide other examples where the three-dimensional dynamics is important. Fully three-dimensional simulations of solar convection with magnetic fields produce flow and magnetic field structures in great detail, but at present they deviate in some important aspects from the Sun (e.g. the fraction of small scale to large scale field is rather large; and the angular velocity contours are still too strongly aligned with the rotation axis). Some tentative explanations are available (magnetic Prandtl number not small enough in the simulations to reduce or even suppress small scale dynamo action, and surface conditions not realistic enough to allow for sufficiently large a baroclinic term). Future advances in computer technology will bring a steady increase in numerical resolution. However, increase of spatial resolution by a factor of two will always be very difficult when close to the machine capacity. Substantial progress may rather hinge on new insights that may emerge from a closer

interrelation between local simulations where turbulence is well resolved and mean field calculations that benefit from input and calibration of detailed simulations.

## Acknowledgements

I thank David Moss and an anonymous referee for making useful suggestions that have helped improving this chapter, and Dr. Y. Kamide for his patience. I apologize again for not having been able to acknowledge, through appropriate references, the many achievements that have been reported here. I have therefore mainly been referencing review material that in turn quote the relevant original work.

## References

- Bahcall, J. N., Basu, S., & Serenelli, A. M., “What Is the Neon Abundance of the Sun?,” *Astrophys. J.* **631**, 1281-1285 (2005)
- Benevolenskaya, E. E., Hoeksema, J. T., Kosovichev, A. G., & Scherrer, P. H., “The interaction of new and old magnetic fluxes at the beginning of solar cycle 23,” *Astrophys. J.* **517**, L163-L166 (1999).
- Brandenburg, A., “The case for a distributed solar dynamo shaped by near-surface shear,” *Astrophys. J.* **625**, 539-547 (2005).
- Brandenburg, A., & Tuominen, I., “Variation of magnetic fields and flows during the solar cycle,” *Adv. Space Sci.* **8**, 185-189 (1988).
- Brandenburg, A., & Subramanian, K., “Astrophysical magnetic fields and nonlinear dynamo theory,” *Phys. Rep.* **417**, 1-209 (2005).
- Brandenburg, A., Moss, D., Rüdiger, G., & Tuominen, I., “The nonlinear solar dynamo and differential rotation: A Taylor number puzzle?” *Solar Phys.* **128**, 243-251 (1990).
- Brandenburg, A., Moss, D., & Tuominen, I., “Stratification and thermodynamics in mean-field dynamos,” *Astron. Astrophys.* **265**, 328-344 (1992).
- Brandenburg, A., Chan, K. L., Nordlund, Å., & Stein, R. F., “Effect of the radiative background flux in convection,” *Astron. Nachr.* **326**, 681-692 (2005).
- Brun, A. S., Miesch, M. S. & Toomre, J., “Global-scale turbulent convection and magnetic dynamo action in the solar envelope,” *Astrophys. J.* **614**, 1073-1098 (2004).
- Christensen-Dalsgaard, J., Duvall, T. L., Jr., Gough, D. O., Harvey, J. W., & Rhodes, E. J., Jr., “Speed of sound in the solar interior,” *Nature* **315**, 378-382 (1985).
- Demarque, P., & Guenther, D. B., “Helioseismology: Probing the interior of a star,” *Proc. Nat. Acad. Sci.* **96**, 5356-5359 (1999).

- Deubner, F.-L., "Observations of low wavenumber nonradial eigenmodes of Sun," *Astron. Astrophys.* **44**, 371-379 (1975).
- Dikpati, M., & Charbonneau, P., "A Babcock-Leighton flux transport dynamo with solar-like differential rotation," *Astrophys. J.* **518**, 508-520 (1999).
- Duvall, T. L., Jr., "A dispersion law for solar oscillations," *Nature* **300**, 242-243 (1982).
- Gailitis, A., Lielausis, O., Platacis, E., et al., "Magnetic field saturation in the Riga dynamo experiment," *Phys. Rev. Letters* **86**, 3024-3027 (2001).
- Gizon, L., & Birch, A. C., "Local Helioseismology," *Living Rev. Solar Phys.* **2** (2005), <http://www.livingreviews.org/lrsp-2005-6>
- Gough, D., "Inverting helioseismic data," *Solar Phys.* **100**, 65-99 (1985).
- Kazantsev, A. P., "Enhancement of a magnetic field by a conducting fluid," *Sov. Phys. JETP* **26**, 1031-1034 (1968).
- Kippenhahn, R. & Weigert, A. *Stellar structure and evolution*. Springer: Berlin (1990).
- Kitchatinov, L. L. & Rüdiger, G., "Differential rotation and meridional flow in the solar convection zone and beneath," *Astron. Nachr.* **326**, 379-385 (2005).
- Krause, F., & Rädler, K.-H. *Mean-Field Magnetohydrodynamics and Dynamo Theory*. Pergamon Press, Oxford (1980).
- Miesch, M. S., Elliott, J. R., Toomre, J., et al., "Three-dimensional spherical simulations of solar convection. I. Differential rotation and pattern evolution achieved with laminar and turbulent states," *Astrophys. J.* **532**, 593-615 (2000).
- Marsh, N., & Svensmark, H., "Cosmic rays, clouds, and climate," *Spa. Sci. Rev.* **94**, 215-230 (2000).
- Mihalas, D. *Stellar Atmospheres*. W. H. Freeman: San Francisco (1978).
- Moffatt, H. K. *Magnetic field generation in electrically conducting fluids*. Cambridge University Press, Cambridge (1978).
- Ossendrijver, M., "The solar dynamo," *Astron. Astrophys. Rev.* **11**, 287-367 (2003).
- Parker, E. N. *Cosmical Magnetic Fields*. Clarendon Press, Oxford (1979).
- Rüdiger, G. *Differential rotation and stellar convection: Sun and solar-type stars*. Gordon & Breach, New York (1989).
- Rüdiger, G. & Brandenburg, A., "A solar dynamo in the overshoot layer: cycle period and butterfly diagram," *Astron. Astrophys.* **296**, 557-566 (1995).
- Rüdiger, G., & Hollerbach, R. *The magnetic universe*. Wiley-VCH, Weinheim (2004).
- Solanki, S. K., Inhester, B., Schüssler, M., "The solar magnetic field," *Rep. Prog. Phys.* **69**, 563-668 (2006).
- Spruit, H. C., "A model of the solar convection zone," *Solar Phys.* **34**, 277-290 (1974).

- Stieglitz, R., & Müller, U., “Experimental demonstration of a homogeneous two-scale dynamo,” *Phys. Fluids* **13**, 561-564 (2001).
- Stix, M., “Comments on the solar dynamo,” *Astron. Astrophys.* **37**, 121-133 (1974).
- Stix, M. *The Sun: an introduction*. Springer-Verlag, Berlin (2002).
- Thompson, M. J., Christensen-Dalsgaard, J., Miesch, M. S., & Toomre, J., “The internal rotation of the Sun,” *Ann. Rev. Astron. Astrophys.* **41**, 599-643 (2003).
- Ulrich, R. K., “The five-minute oscillations on the solar surface,” *Astrophys. J.* **162**, 993-1002 (1970).